NACA

RESEARCH MEMORANDUM

for

U. S. Army Ordnance

LONGITUDINAL AERODYNAMIC CHARACTERISTICS AND EFFECT OF

ROCKET JET ON DRAG OF MODELS OF THE HERMES A-3A

AND A-3B MISSILES IN FREE FLIGHT AT

MACH NUMBERS FROM 0.6 TO 2.0

By H. Herbert Jackson

Langley Aeronautical Laboratory
Langley Field, Va.

CLASSIFIED DOCUMENT

This document contains classified information affecting the National Defense of the United States within the meaning of the Espionage Act, USC 18:793 and 794. Its transmission or the revelation of its contents in any manner to an unauthorized person is prohibited by law.

NATIONAL ADVISORY COMMITTEE
FOR AERONAUTICS
WASHINGTON

JUN 29 1955

CONFIDENTIAL

NATIONAL ADVISORY COMMITTEE FOR AERONAUTICS

RESEARCH MEMORANDUM

for

U. S. Army Ordnance

LONGITUDINAL AERODYNAMIC CHARACTERISTICS AND EFFECT OF

ROCKET JET ON DRAG OF MODELS OF THE HERMES A-3A

AND A-3B MISSILES IN FREE FLIGHT AT

MACH NUMBERS FROM 0.6 TO 2.0

By H. Herbert Jackson

SUMMARY

A free-flight investigation over a Mach number range from 0.6 to 2.0 has been conducted to determine the longitudinal aerodynamic characteristics and effect of rocket jet on zero-lift drag of 1/5-scale models of two ballistic-type missiles, the Hermes A-3A and A-3B.

Models of both types of missiles exhibited very nearly linear normal forces and pitching moments over the angle-of-attack range of 8° to -4° and Mach number range tested. The centers of pressure for both missiles were not appreciably affected by Mach number over the subsonic range; however, between a Mach number of 1.02 and 1.50 the center of pressure for the A-3A model moved forward 0.34 caliber with increasing Mach number. At a trim angle of attack of approximately 3°, the A-3A model indicated a total drag coefficient 30 percent higher than the power-off zero-lift drag over the subsonic Mach number range and 10 percent higher over the supersonic range.

Under the conditions of the present test, and excluding the effect of the jet on base drag, there was no indicated effect of the propulsive jet on the total drag of the A-3A model. The propulsive jet operating at a jet pressure ratio p_j/p_o of 0.8 caused approximately 100-percent increase in base drag over the Mach number range $M = 0.6$ to 1.0. This increase in base drag amounts to 15 percent of the total drag. An under-expanded jet operating at jet pressure ratios corresponding approximately to those of the full-scale missile caused a 22-percent reduction in base drag at $M = 1.55$ $\left(p_j/p_o = 1.76\right)$ but indicated no change at $M = 1.30$ $\left(p_j/p_o = 1.43\right)$. At $M = 1.1$ and $p_j/p_o = 1.55$, the jet caused a 50-percent increase in base drag.

CONFIDENTIAL

INTRODUCTION

The Hermes A-3A and A-3B missiles have been designed by the General Electric Company as prototype surface-to-surface missiles for close support of ground troops, and each was designed for high accuracy. In order to predict the range and guidance system tolerances more closely and to define the center-of-pressure curves of the missiles more precisely, six 1/5-scale models, four of the Hermes A-3A and two of the Hermes A-3B, were flight tested at the Langley Pilotless Aircraft Research Station at Wallops Island, Va.

The effects of a propulsive jet on the external drag of the missiles were investigated by flight testing three Hermes A-3A models (designated herein as models A(1), A(2), and A(3)) and one Hermes A-3B model (designated herein as model B) at ratios of jet-exit static pressure to free-stream static pressure similar to those expected on the full-scale missiles. Since, to date, there is no completely adequate theoretical approach to the prediction of the quantitative effects of the jet, total reliance has been placed on experiment. Some data as to these effects are presented in references 1, 2, and 3 and systematic studies of various phases of the general subject at supersonic speeds are presented in references 4 to 8. The data presented herein are more nearly complete than those presented in reference 1.

One A and one B model were flight tested to determine aerodynamic characteristics of the missiles at subsonic, transonic, and supersonic speeds. Longitudinal stability, trim, and drag were obtained from an analysis of continuous telemeter records, of velocity radar, and of short-period oscillations induced by pulse rockets.

The data are presented over a Mach number range of 0.6 to 2.0 and cover a Reynolds number range of 15×10^6 to 85×10^6 based on body length.

SYMBOLS

c_{D_T} total drag coefficient, based on maximum cross-sectional area of body

c_{D_B} base drag coefficient, referred to maximum cross-sectional area of body; for power on, $\dfrac{p_b - p_o}{q_o} \dfrac{A_a}{A_{max}}$; for power off, $\dfrac{p_b - p_o}{q_o} \dfrac{A_b}{A_{max}}$

C_T thrust coefficient, $T/q_0 A_{max}$

C_N normal-force coefficient, $\left(\dfrac{a_n}{g} \dfrac{W}{q_0 A_{max}} \right)$

C_Y side-force coefficient, $\left(\dfrac{a_y}{g} \dfrac{W}{q_0 A_{max}} \right)$

C_R resultant-force coefficient,

$$\left[\left(C_N - C_{N_{trim}} \right)^2 + \left(C_Y - C_{Y_{trim}} \right)^2 \right]^{1/2}$$

C_m total pitching-moment coefficient about missile center of gravity

$\dfrac{p_b - p_0}{q_0}$ base pressure coefficient

$\dfrac{\Delta p}{q_0}$ side-pressure coefficient

q dynamic pressure, lb/sq ft

p pressure, lb/sq ft

T thrust, lb

D drag, lb

a acceleration as obtained from accelerometer, ft/sec^2

g acceleration due to gravity, ft/sec^2

γ ratio of specific heats

d maximum body diameter (1 caliber); 0.667 ft for A models, 0.783 ft for B models

W model weight, lb

m mass, W/g, slugs

M Mach number

R   Reynolds number based on body length; 5.733 ft for A models, 6.617 ft for B models

A_{max} maximum cross-sectional area of body; 0.349 sq ft for A models, 0.482 sq ft for B models

A_a annular area between rocket nozzle and model base, 0.0767 sq ft

A_b total base area, 0.126 sq ft

A_e nozzle-exit area, sq ft

A_t nozzle-throat area, sq ft

I_Y moment of inertia about Y-axis, slug-ft^2

I_Z moment of inertia about Z-axis, slug-ft^2

I_X moment of inertia about X-axis, slug-ft^2

α angle of attack, deg

δ nozzle-divergence half-angle, deg

λ thrust correction for nozzle divergence, $\frac{1}{2}(1 + \cos \delta)$

δ_H horizontal fin incidence, deg

$\dot{\phi}$ roll velocity, radians/sec

θ angle of pitch, radians

$C_{m_q} = \dfrac{dC_m}{d\left(\dfrac{q\bar{c}}{2V}\right)}$, per radian

$C_{m_{\dot{\alpha}}} = \dfrac{dC_m}{d\left(\dfrac{\dot{\alpha}\bar{c}}{2V}\right)}$, per radian

Subscripts:

b   base

cg   center of gravity of missile

j   jet

n   normal

o   free stream

t   nozzle throat

y   transverse

$$\dot{\alpha} = \frac{1}{57.3} \frac{d\alpha}{dt}$$

$q = \frac{d\theta}{dt}$, when used in the damping term

The symbols α, $\dot{\alpha}$, q used as subscripts indicate the derivative of the quantity with respect to the subscript; for example, $C_{N_\alpha} = \frac{dC_N}{d\alpha}$.

MODELS AND APPARATUS

The test bodies used to obtain the data presented herein were bodies of revolution having cruciform tail fins. Sketches showing the external details of the stability models are presented in figure 1. The drag models differed from the stability models, as can be seen from the photographs in figure 2, in that no total-pressure tubes or angle-of-attack stings and indicators were used on the drag models. Also jet vanes were fixed to the bases of the drag models, although none were used on the stability models. Photographs of the tail sections of the drag models showing the location of the jet vanes and pressure orifices are presented in figure 3.

The models were constructed of laminated mahogany with aluminum-alloy tail sections and fins. The stability models had steel nose plugs from which protruded the angle-of-attack sting, whereas the drag models had brass nose plugs for ballast. The wood portions of drag models A(1) and A(2) were finished with clear lacquer, whereas all other models were finished with a commercial preparation that is able to withstand the aerodynamic heating associated with supersonic Mach numbers below Mach number 2.5.

The A models, which consisted of an L-V Haack nose with fineness ratio of 5.6 extending back to the maximum-body diameter and a circular-arc section that faired into a cone-frustum tail, had a fineness ratio of 8.6 and a body maximum cross-sectional area of 0.349 sq ft. The B models, which were made up of a nose cone of approximately 31.5° apex angle and frustums of cones, had a fineness ratio of 8.45 and a body maximum cross-sectional area of 0.482 sq ft.

Four fins having double-wedge airfoil sections, triangular plan forms with leading-edge sweepback of 60° and aspect ratio of 2.3, and the maximum thickness at 65 percent chord were mounted in a cruciform arrangement at the base of each model. Two of the diametrically opposed fins (normal to the plane in which the pulse rockets were fired) on stability model A were fixed at -2.05° incidence, leading edge down, whereas the fins in the vertical plane had no incidence. All fins on stability model B and on the drag models had zero degree of deflection. As can be seen from figure 1, the B models had fins which were approximately 30 percent larger in area than those of the A models. These larger fins were also used on drag model A(3).

In order to simulate full-scale test conditions as closely as possible, 1/5-scale, SAE 1020 steel, nonmovable jet vanes, each having a planform area of 0.72 sq in., were fixed into the base of the jet-effect models as shown in figures 2 and 3. The type of jet vanes used can more easily be seen from figure 4 which shows two jet vanes prior to and after being used in the static test of a sustainer rocket motor. As shown by figure 4, drag models A(3) and B had flame-deflector plates attached to the jet vanes to prevent melting of the trailing edge of the stabilizing fins. The trailing edge of the stabilizing fins for drag models A(3) and B protruded 0.75 inch rearward of the base of each model.

A two-stage propulsion system was employed for all models presented herein, and all models utilized a modified 5-inch British Cordite rocket motor as the sustainer unit. Various booster rocket motors were utilized to obtain the Mach numbers desired. Drag models A(1), A(2), A(3), and B used a 3.25-inch Mk 7 aircraft rocket motor, a 5-inch HVAR lightweight, a 65-inch-long HVAR, and a 6.25-inch ABL Deacon rocket motor, respectively, as booster rockets. Both stability models utilized 65-inch-long HVAR motors as boosters. All boosters were equipped with four stabilizing fins. Shown in figure 5 is the model-booster combination for stability Model B on the launching stand. The modifications to the sustainer motor used in the drag models varied with the model and are shown in figure 6.

Four pulse rockets thrusting normal to the body axis were installed in the nose of each stability model. The locations of the pulse rockets are shown in figure 1. Each pulse rocket had a total impulse of approximately 8 pound-seconds and a burning time of approximately 0.08 second.

Physical characteristics of the stability models, after burnout of the sustainer rocket motor, are presented in the following table:

	Model A	Model B
Center of gravity, calibers aft of station 0 . .	5.377	4.869
Weight, lb	91.50	116.00
I_Y, slug-ft^2	7.063	14.754
I_Z, slug-ft^2	7.111	14.746
I_X, slug-ft^2	0.184	0.284

Each model was equipped with an NACA telemetering system which transmitted continuous flight measurements to the ground receiving station. Velocity and total drag were obtained from CW Doppler radar as described in reference 9 and from telemetered data. Trajectory and atmospheric data were obtained from an SCR 584 tracking radar unit and by radiosonde observations made at the time of launching.

Approximate values of the rate-of-roll of the stability models were obtained by a spinsonde receiver in conjunction with the telemeter antennas which were plane-polarized. Even though the spinsonde yields only an average value of $\dot{\phi}$ for a finite time interval, it is believed to be a good indication of the level of the rate of roll.

TESTS AND ANALYSIS

Tests

The variation of the test conditions, Reynolds number and dynamic pressure, with Mach number for the test models are shown in figures 7 and 8, respectively. The Reynolds numbers shown in figure 7 are based on body length.

The base pressure measurements for the drag models were made using one pressure orifice on the base annulus, 45° between the fins and jet vanes as shown in figure 3. Side pressure was measured by an orifice located 45° between the fins, 1 base diameter (4.8 in.) forward of the base for drag model A(1) and 1/2 base diameter (2.4 in.) forward of the base for drag model A(2). The sustainer-rocket-motor chamber pressure for the models was measured by an orifice located at the beginning of the convergent section of the nozzle. The rocket-motor-exit static pressure was obtained from measurements at an orifice located ahead of the nozzle exit, and then corrected to exit condition.

All the rocket motors were static tested prior to flight testing to obtain a correlation of measured thrust with rocket chamber pressure and exit static pressure. The rocket motors used in the static tests were also used in the flight tests, with the sustainer grain weights and characteristics remaining the same for both tests. In order to simulate closely actual flight conditions in the static tests, each test was run with jet vanes in place. It was shown in the static tests that each vane had an average loss in effective area, due to thermal shock, erosion, melting, and oxidation of approximately 15 percent and an average loss in weight of about 1.2 percent of the initial vane weight. This loss in effective area is about what would be expected on the full-scale missile.

Analysis

The technique of data reduction for an analysis of the response of models to abrupt disturbances is described in reference 10 for abrupt elevator deflections. The method applies equally well for models employing pulse rockets such as stability models A and B. Briefly, however, static longitudinal stability is determined from the periods of the short-period oscillations and dynamic longitudinal stability is determined from the rate of decay of the oscillations. The oscillations occurring during pulse rocket burning are not included in the analysis because the time history of the thrust-forcing function cannot be evaluated accurately. The angles of attack measured by the indicators shown in figure 1 were corrected to angles of attack at the center of gravity of the models by the method of reference 11. The two-accelerometer method for obtaining instantaneous total pitching-moment coefficients was used as described in reference 12. All measurements used for the stability models were taken during the decelerating portion of the flight.

In order to evaluate the effect of the jet on the drag models, it was necessary to determine the drag of the models during power-on. This can be done by knowing the thrust and net acceleration of the configuration and evaluating the drag according to the equation

$$D = T - \frac{W}{g}(a) \tag{1}$$

The thrust of the flight models may be determined from the flight measurements of the jet-exit pressure and rocket-chamber pressure, whereas the acceleration is measured directly by longitudinal accelerometers. Because of the high ratios of thrust to drag for the models, the accuracy in determining the power on drag is critically related to the accuracy in computing the thrust.

As indicated in reference 3, the thrusts of other modified Cordite rocket motors first calibrated in preflight static tests and then calculated from the equation

$$T = p_j A_j \left(\lambda \gamma_j M_j^2 + 1 \right) - p_o A_j \qquad (2)$$

show good agreement, with any differences being of a random nature. Applying the equation, however, to the rocket motors used in the present (drag) tests, resulted in calculated static thrusts higher than those measured during the static test of each motor. It was assumed that, since jet vanes were attached to the rocket motors during the ground tests and since equation (2) does not account for the presence of the vanes, the lower measured thrusts were due to thrust loss caused by the jet vanes. Using the thrusts as calculated by equation (2) in the equation for determining dynamic pressures of the jet at the exit

$$q_j = \frac{1}{2\lambda} \left[\frac{T}{A_j} - \left(p_j - p_o \right) \right] \qquad (3)$$

and using the zero-lift vane drag coefficients indicated in reference 13, it was possible to obtain vane drags equivalent to the difference in calculated and measured thrusts.

The thrust coefficients, based on body frontal area, obtained from flight measurements are presented against Mach number in figure 9. The thrust coefficient shown for model A(1) covers only a Mach number range of 0.8 to 1.0 because of malfunctioning of the flight chamber pressure pickup below Mach number 0.8.

Shown in figure 10 is the variation of p_j/p_o, the ratio of jet-exit pressure to free-stream pressure, as a function of flight Mach number. Also shown for comparison are plots of p_j/p_o corresponding to possible trajectories of the full-scale missiles.

Accuracy

The accuracy of the measured quantities is difficult to establish because the instrumentation calibrations cannot be checked during or after the flight. Most of the probable instrumentation errors occur as errors in absolute magnitude. Incremental values or slopes should, in general, be more accurate than absolute values. Converted to coefficient form, the maximum estimated errors in the normal-force coefficient and angle of attack are as follows:

M	Error in C_N		Error in α, deg	
	Model A	Model B	Model A	Model B
1.5	0.006		0.14	
1.1	.010	0.008	.14	0.16
.8	.038	.015	.14	.16

The CW Doppler radar unit is believed to be accurate to better than 1 percent for nonmaneuvering models. The Mach number at peak velocity and during those times in which the models have trimmed out should therefore be accurate to 1 percent or better.

The error in the faired curves of total drag coefficient (power off) and base drag coefficient (power on and off) presented herein is believed to be less than ±0.007 and ±0.005, respectively. As stated previously, the error in power-on total drag coefficient is dependent upon the accuracy with which the thrust coefficient C_T can be determined. By taking into account the thrust loss due to the jet vanes, it is believed possible to obtain power-on total drag coefficients within an accuracy of ±0.014 or twice the error of the power-off total drag coefficient.

Further errors in the aerodynamic coefficients may arise from possible dynamic-pressure inaccuracies which are approximately twice as great as errors in Mach number. Errors in angle of attack are independent of dynamic pressure and are not likely to vary with Mach number.

An indication of random errors encountered may be noted from the scatter of data points shown in the figures.

Normal Force and Pitching Moment

The variations of C_N with angle of attack for stability models A and B are shown in figures 11(a) and 11(b), respectively. Shown in figure 12 are the variations of C_m with C_N for the two models. The plots shown in figures 11 and 12 are only sample plots, taking one oscillation from each of a series of oscillations resulting from the firing of pulse rockets. As shown by the plots, both models exhibited very nearly linear normal forces and pitching moments over the angle-of-attack range of $8°$ to $-4°$ and Mach number range tested.

The normal-force-curve slopes at trim C_N, represented by the faired curves in figure 11, are presented as functions of Mach number in figure 13 for both stability models. As shown in figure 13(a) there was very little change of C_{N_α} for model A over the Mach number range tested. The C_{N_α} for model B is indicated by figure 13(b) as smoothly increasing from a subsonic value of 0.1 at $M = 0.90$ to 0.125 at $M = 1.05$. Also shown in 13(b) for comparison are subsonic data obtained in the Langley low-turbulence pressure tunnel (ref. 14). As can be seen from the figure, the agreement between free-flight data and data of reference 14 is excellent.

Static Longitudinal Stability

The trim normal-force coefficients for the two configurations through the usable Mach number range are shown in figure 14(a). The transition from subsonic to supersonic flight appears quite smooth for both stability models with model A $\left(\delta_H = 2.05^0\right)$ indicating trim normal-force coefficient increasing from 0.26 at $M = 0.95$ to 0.29 at $M = 0.71$. Model B which had all four fins fixed at 0^0 incidence shows a trim normal-force coefficient of 0 over the Mach number range shown.

Angles of attack corresponding to these trim normal-force coefficients are shown in figure 14(b). The 2.05^0 incidence in the horizontal fins of the A model caused a subsonic trim angle of attack of about 3^0 which gradually increased with increasing Mach number to a supersonic value of 3.6^0. The trim angle of attack for model B was approximately 0^0 over the entire Mach number range.

Shown in figure 15 is the variation with Mach number of the static-longitudinal-stability parameter dC_m/dC_N in calibers from the center of gravity, as obtained from the normal accelerometers a known distance apart and the equation

$$\frac{dC_m}{dC_N} = \frac{I_Y}{l \ dm} \left(\frac{\dfrac{da_{n_{nose}}}{g}}{\dfrac{da_{n_{cg}}}{g}} - 1 \right)$$

where l is the distance between the two accelerometers. The centers of gravity were 5.377 and 4.869 calibers from body station 0 for models A and B, respectively. The test data points shown in figure 15 give an indication of the scatter which was obtained by this method. As can be seen from the figure, stability models A and B were both longitudinally stable over the test Mach number range for the centers of gravity used.

Utilizing the faired curves of dC_m/dC_N as obtained by the two-accelerometer method, it was possible to obtain the variation of missile center of pressure with Mach number for models A and B shown by the solid curves in figure 16. For comparison and to give an indication of the scatter which might be expected in determining free-flight center of pressure by various methods, center-of-pressure data points as obtained by two additional methods are shown in figure 16. These two methods were carried out

(a) By measuring periods of the short-period oscillations for each missile and then converting these data to the static-stability parameter C_{m_α}. The static-stability parameters determined were then combined with the known normal-force-coefficient slopes, shown in figure 13, to obtain center-of-pressure locations.

(b) By determining the slopes of the total pitching-moment coefficients with normal-force coefficients as shown in figures 12(a) and 12(b) and then converting the slopes to center of pressure. The total pitching-moment coefficients used in this method were obtained by the two-accelerometer method described in reference 12.

Although there was some scatter present in figures 12(a) and (b), particularly at low Mach numbers, generally, as can be seen from figure 16 the data agreed with the slopes of the period method. As shown by figure 16, the agreement between the three methods of determining the center of pressure was quite good. The center of pressure in calibers from the nose for model A, $\delta_H = 2.05^\circ$, is indicated as increasing in value from 6.63 at $M = 0.75$ to 6.72 at $M = 1.02$ and then decreasing to 6.38 at $M = 1.50$. For model B, $\delta = 0^\circ$, the center of pressure is indicated as increasing from a value of 6.30 at $M = 0.90$ to 6.38 at $M = 1.10$. The subsonic center of pressure for model B is indicated as being slightly more rearward than the data from reference 14.

Dynamic Longitudinal Stability

The times required for the short-period oscillations of the A and B stability models to damp to one-half amplitude are shown in figure 17. The scatter of points for model B may be due to that model having more noticeable cross-coupling of lateral and pitching moments than model A.

The variations of $C_{m_q} + C_{m_{\dot\alpha}}$ with Mach number shown in figure 18 were obtained from analysis of the damping of the resultant oscillations from trim of each stability model. Analysis of the resultant oscillations, as obtained from C_R, was necessitated by the roll displacement which occurred during the longitudinal oscillations. The curve for model A is

composed of four points, one from the damping of each pulse rocket firing. The curve for model B is composed of only three points because of the high rate of roll generated by the model at the last pulse rocket firing.

The longer fin normal-force moment arm and 30-percent larger fins of model B would both combine to increase the damping of model B over that of model A, as is indicated in figure 18. The damping of the two missiles was influenced by C_{N_α} to the extent that a 2-percent error in C_{N_α} at $M = 0.96$ would cause a 2-percent and 1-percent error in $C_{m_q} + C_{m_{\dot{\alpha}}}$ for models A and B, respectively. The calculated values indicated at $M = 1.0$ are 110 and 206 for models A and B, respectively.

Throughout the flights of both stability models, each model exhibited lateral oscillations when pulsed in pitch. These lateral oscillations, although evident for model A, were of very small amplitude in comparison with the longitudinal oscillation and may have been initially caused by the thrust line of the pulse rockets being slightly off from the longitudinal axis. The lateral oscillations for stability model B were also of very small amplitude until the model had decelerated to a Mach number of 0.75. At this point the amplitude of the lateral oscillation became greater than that of the longitudinal oscillation. The resulting motions were such that no further useful longitudinal stability data could be obtained.

Stability model A had an indicated rate of roll, as obtained by a spinsonde receiver, of ±0.5 radian per second, which is less than the accuracy of ±1.0 radian per second of this method. For stability model B, the indicated rate of roll between Mach numbers 1.2 and 0.9 was 1.25 radians per second. Below a Mach number of 0.9, model B had an indicated $\dot{\varphi}$ varying between ±3.5 radians per second.

Drag

The total drag coefficients at trim lift coefficients throughout the test Mach number ranges are shown for stability models A and B in figure 19.

The total drag coefficient at trim from stability model A, as indicated by figure 19(a), is higher than the zero-lift drag (power off), shown in reference 1 and figure 20 herein, by about 30 percent over the subsonic range and 10 percent over the supersonic range of the test. The total drag coefficient at a trim angle of attack of about 3.0° is indicated as having a value of 0.13 at $M = 0.7$, increasing to 0.263 at $M = 1.025$, with the most abrupt increase near $M = 0.925$. Because of malfunctioning of the longitudinal accelerometer in stability model A, it was impossible to determine minimum drag values and the drag coefficients at trim shown were obtained from Doppler radar data.

The drag coefficient at trim for stability model B, as indicated by
figure 19(b), is in very good agreement with subsonic data from the Langley
low-turbulence pressure tunnel (ref. 14). Stability model B is indicated
as having a subsonic drag coefficient of 0.10 increasing to 0.325 at
$M = 1.07$ and decreasing to 0.290 at $M = 1.25$ with the most abrupt drag
rise occurring near $M = 0.875$.

Presented in figure 20 are total and base drag coefficients (power
on and power off) for the A drag models tested. The power-off total and
base drags are shown by faired curves. In order to make a total-drag
comparison between the three A models tested, the total drag coefficients
of model A(3) were corrected for the previously mentioned increased fin
area. This was done with the aid of reference 15, and the resulting
power-off drag was indicated in reference 1 as being in good agreement
with model A(2). Because of failure of the B drag model at sustainer
rocket-motor burnout, no power-off data are presented for the model.

It was indicated for the A drag models that, when the effects of the
jet vane drag were taken into account, the power-on and power-off total
drag coefficients agreed within the previously quoted power-on total-
drag-coefficient accuracy of ±0.014 over the entire Mach number and p_j/p_o
range tested. For this reason, the power-on and power-off total drag
coefficients are represented by the same faired curve.

The drag-coefficient increments due to the jet vanes were arrived
at by using a vane drag coefficient of 0.18, as obtained from reference 13,
and assuming that thermal shock on the sharp vane leading edge reduced
the area of each vane from 0.72 to 0.612 square inch, or 15 percent, imme-
diately on firing the rocket motor. The vane drags obtained after deter-
mining the rocket jet dynamic pressure were converted to an incremental
drag coefficient by basing it on free-stream conditions. The jet flow
acting on the jet vanes caused vane drag that amounted to as much as
48 percent of the total drag at $M = 0.95$, 24.8 percent at $M = 1.051$,
and 25.3 percent at $M = 1.1$, for models A(1), A(2), and A(3), respec-
tively. For model A(3), the vane drag varied from 25.3 to 16.8 percent
of the total drag at $M = 1.1$ to 1.56, respectively.

As can be seen from figure 20, there are noticeable interference
effects of the jet flow on the base drag of the A drag models. The sub-
sonic power-on base drag of model A(1), with an overexpanded jet
$\left(p_j/p_o < 1\right)$, is indicated as being more than twice the power-off base
drag, or an increase amounting to 15 percent of the total drag, although
the annulus area was but 60 percent of the total base area. The jet flow
decreased the base drag over the Mach number range of 0.9 to 1.045 and
1.3 to 1.77 for models A(2) and A(3), respectively. There was no indicated
effect of jet flow on the base drag of model A(2) at $M = 1.3$ $\left(p_j/p_o = 1.43\right)$,

where the jet pressure ratio of the model corresponds to that of the full-scale A-3A missile. The jet flow caused the base drag of model A(3) to be increased 50 percent at $M = 1.1$ $\left(p_j/p_o = 1.55\right)$ and a 22-percent reduction at $M = 1.55$ $\left(p_j/p_o = 1.76\right)$ where the jet pressure ratio of the model matches that of the full-scale A-3A missile.

It is indicated by figure 21, which shows the effect of the jet on the side-pressure coefficient, that there was no appreciable effect of the jet flow from the base on the afterbody pressures, 45° between the fins and within 1/2 base diameter of the base. It is not impossible, however, that the afterbody pressures closer to the base and in the region of the fins (where the fin interference effects would be the largest) would be affected to a greater extent than those measured 45° between the fins. The areas over which such pressures could act would however be small, allowing for negligible effect on total drag.

Shown in figure 22 is a comparison of the power-off base pressure coefficient with the power-on base pressure coefficients measured at the various p_j/p_o ratios tested. The power-off data are shown by one faired curve. There was a maximum scatter of ±0.004 in base pressure coefficient over those Mach numbers covered by the overlap of data from model A(2) and A(3). The power-off values indicated at $M = 1.59$ are substantiated by those presented in reference 4. The data presented in reference 4, however, are for models without jet vanes and with a different A_j/A_t ratio than that used in the models presented herein, making it impractical to make any comparison of power-on data.

The power-on base-pressure-coefficient curves presented for the A models shows that, except for model A(2) between $M = 0.85$ and 1.02, the propulsive jet caused considerable reductions in base pressure over the jet pressure ranges tested. Assuming, since the afterbodies of the A and B models are the same, that the power-off base pressure coefficients would also be the same, it is shown by figure 22 that the propulsive jet at a jet pressure ratio of 2.1 caused power-on base pressures to be higher than those with power off. At $M = 1.5$, the indicated power-on base pressure coefficient for the B model would mean a reduction of 0.016 or 48 percent in base drag coefficient due to jet flow from the base.

CONCLUSIONS

A flight investigation of the aerodynamic characteristics and effect of rocket jet on zero-lift drag of two rocket-powered missile configurations, the Hermes A-3A and A-3B, over the Mach number range of 0.6 to 2.0 has indicated the following:

1. Both models exhibited very nearly linear normal forces and pitching moments over the tested Mach number range and angle-of-attack range of 8° to -4°.

2. The centers of pressure for both models were not appreciably affected by Mach number over the subsonic range. For the A-3A model, the center of pressure moved forward with increasing Mach numbers from a point 6.72 calibers from the model nose at $M = 1.02$ to 6.38 calibers at $M = 1.50$.

3. The damping-in-pitch derivatives $C_{m_q} + C_{m_{\dot\alpha}}$ for the A-3B model with 0° trim angle of attack were about twice those of the A-3A model with a trim angle of attack of about 3°.

4. The drag coefficients at a trim angle of attack of about 3° for the A-3A model were 10 percent and 30 percent higher than the zero-lift drag over tested supersonic and subsonic ranges, respectively. The drag coefficient at trim angle of attack of about 3.0° increased from 0.13 at subsonic speeds to 0.263 at $M = 1.025$. For the A-3B model, the drag coefficient at 0° trim increased from 0.10 at subsonic speeds to 0.325 at $M = 1.07$.

5. In the subsonic and transonic Mach number range of the present tests, a jet having a jet pressure ratio $\left(p_j/p_o\right)$ of 0.8 influenced the base pressure in such a manner as to increase the base drag of the A-3A model 100 percent or an amount equal to 15 percent of the total drag. The propulsive jet of the A-3A model at jet pressure ratios corresponding to those of the full-scale missile showed no effect on the base drag at $M = 1.30$ $\left(p_j/p_o = 1.43\right)$; however, the base drag was lowered 22 percent at $M = 1.55$ $\left(p_j/p_o = 1.76\right)$. At $M = 1.1$ and $p_j/p_o = 1.55$, the jet caused a 50-percent increase in base drag.

6. Under the conditions of the present test, and excluding the effect of the jet on base drag, there was no indicated effect of the propulsive jet on the total drag of the A-3A model.

Langley Aeronautical Laboratory,
    National Advisory Committee for Aeronautics,
        Langley Field, Va., June 9, 1955.

                                        H. Herbert Jackson
                                        Aeronautical Research Scientist
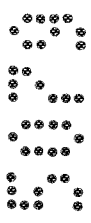
Approved:
            Joseph A. Shortal
    Chief of Pilotless Aircraft Research Division

rmw

REFERENCES

1. Jackson, H. Herbert: Effect of Rocket-Motor Operation on the Drag
      of Three 1/5-Scale Hermes A-3A Models in Free Flight. NACA
      RM SL54B04, Ordnance Dept. 1954.

2. Purser, Paul E., Thibodaux, Joseph G., and Jackson, H. Herbert: Note
      on Some Observed Effects of Rocket-Motor Operation on the Base
      Pressures of Bodies in Free Flight. NACA RM L50I18, 1950.

3. DeMoraes, Carlos A.:   Transonic Flight Test of a Rocket-Powered Model
      To Determine Propulsive Jet Influence on the Configuration Drag.
      NACA RM L54D27, 1954.

4. DeMoraes, Carlos A., and Nowitsky, Albin M.:   Experimental Effects
      of Propulsive Jets and Afterbody Configurations on the Zero-Lift
      Drag of Bodies of Revolution at a Mach Number of 1.59. NACA
      RM L54C16, 1954.

5. Cortright, Edgar M., Jr., and Kochendorfer, Fred D.:   Jet Effects on
      Flow Over Afterbodies in Supersonic Stream. NACA RM E53H25, 1953.

6. Love, Eugene S.:   Aerodynamic Investigation of a Parabolic Body of
      Revolution at Mach Number of 1.92 and Some Effects of an Annular
      Jet Exhausting From the Base. NACA RM L9K09, 1950.

7. Love, Eugene S., and Grigsby, Carl E.:   Some Studies of Axisymmetric
      Free Jets Exhausting From Sonic and Supersonic Nozzles Into Still
      Air and Into Supersonic Streams. NACA RM L54L31, 1955.

8. Henry, Beverly Z., Jr., and Cahn, Maurice S.:   Preliminary Results
      of an Investigation at Transonic Speeds To Determine the Effects
      of a Heated Propulsive Jet on the Drag Characteristics of a Related
      Series of Afterbodies. NACA RM L55A24a, 1955.

9. Wallskog, Harvey A., and Hart, Roger G.:   Investigation of the Drag
      of Blunt-Nosed Bodies of Revolution in Free Flight at Mach Numbers
      From 0.6 to 2.3. NACA RM L53D14a, 1953.

10. Gillis, Clarence L., Peck, Robert F., and Vitale, A. James: Prelim-
      inary Results From a Free-Flight Investigation at Transonic and
      Supersonic Speeds of the Longitudinal Stability and Control Char-
      acteristics of an Airplane Configuration With a Thin Straight Wing
      of Aspect Ratio 3. NACA RM L9K25a, 1950.

11. Mitchell, Jesse L., and Peck, Robert F.: An NACA Vane-Type Angle-of-
    Attack Indicator for Use at Subsonic and Supersonic Speeds. NACA
    TN 3441, 1955. (Supersedes NACA RM L9F28a.)

12. Vitale, A. James: Effects of Wing Elasticity on the Aerodynamic
    Characteristics of an Airplane Configuration Having 45° Sweptback
    Wings As Obtained From Free-Flight Rocket-Model Tests at Transonic
    Speeds. NACA RM L52L30, 1953.

13. Giladett, Leo V., and Wineman, Andrew R.: Investigation of Vanes
    Immersed in the Jet of a Solid-Fuel Rocket Motor. NACA RM L52F12,
    1952.

14. Burrows, Dale L., and Newman, Ernest E.: Wind-Tunnel Tests of a
    Model of a Wingless Fin-Controlled Missile To Obtain Static Sta-
    bility and Control Characteristics Through a Range of Mach Numbers
    From 0.5 to 0.88. NACA RM L53J06, 1954.

15. Welsh, Clement J.: Results of Flight Tests To Determine the Zero-
    Lift Drag Characteristics of a 60° Delta Wing With NACA 65-A006
    Airfoil Section and Various Double-Wedge Sections at Mach Numbers
    From 0.7 to 1.6. NACA RM L50F01, 1950.

Model A

Line of pulse
rocket thrust

Total-pressure
tube

10.000

60°

4.5°

8.000

8.750

r

4.80

17.880

d

93.408

2.05°

x

8.329

L

50.820

68.800

Sta. 0

$$r = \frac{d}{2} \sqrt{\frac{1}{\pi} \left(\emptyset - \frac{1}{2} \sin 2\emptyset + c_1 \sin^3 \emptyset \right)}$$

$$\emptyset = \cos^{-1} \left(1 - \frac{2x}{L} \right)$$

L = 44.82
d = 8.00
c_1 = 1/3

c

0.65c

0.05c

Typical fin section

Model B

Angle-of-attack indicator

Line of pulse
rocket thrust

Total-pressure tube

12.000

60°

4.5°

3.211

8.994

9.400

9.312

7.633

4.800

20.544

7.375

8.329   5.700

24.509

30.200

32.600

56.200

79.400

0.75

Sta. 0
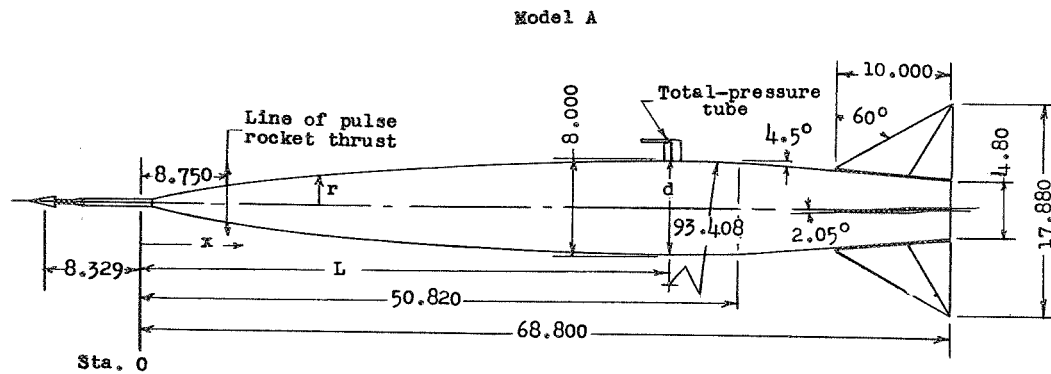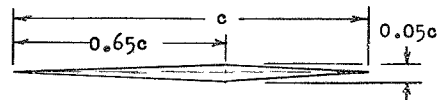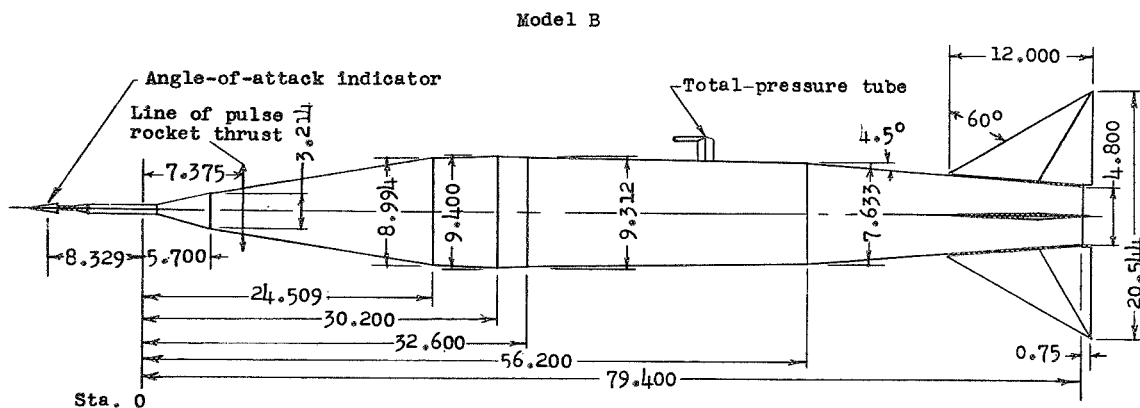
Figure 1.- General arrangements of stability test models. Linear
dimensions are in inches.
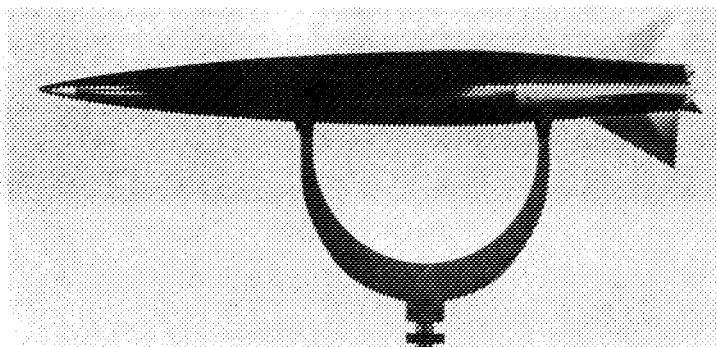
(a) Drag model A(1).
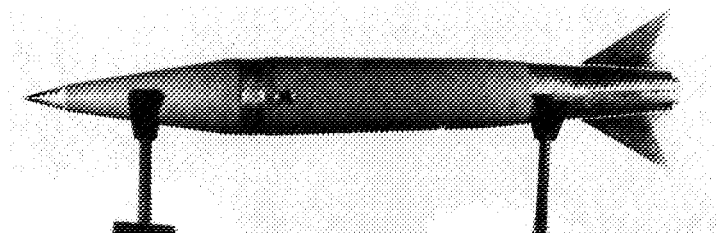
(b) Drag model B.
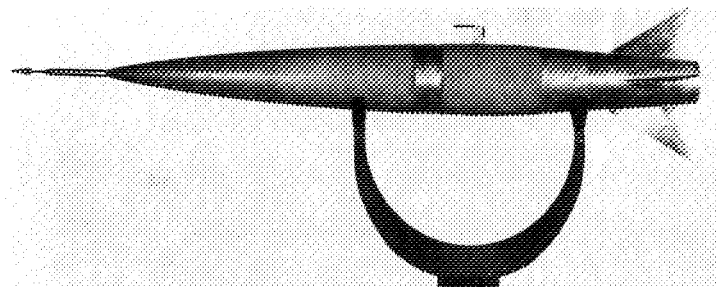
(c) Stability model A.
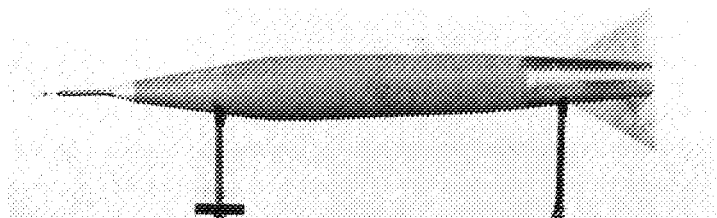
(d) Stability model B.   L-89337

Figure 2.- General views of test models.
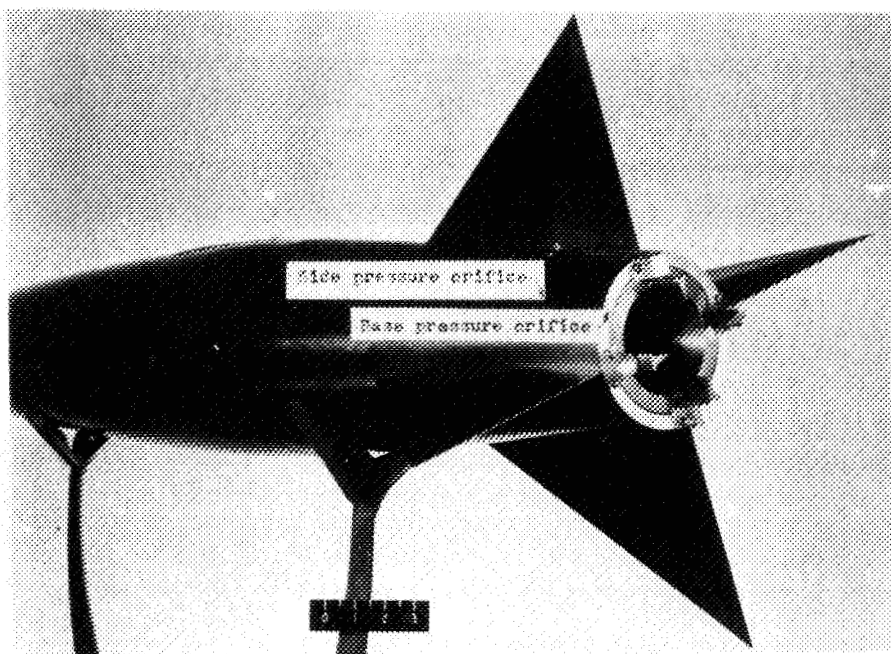
(a) Model A(1).   L-71448.1
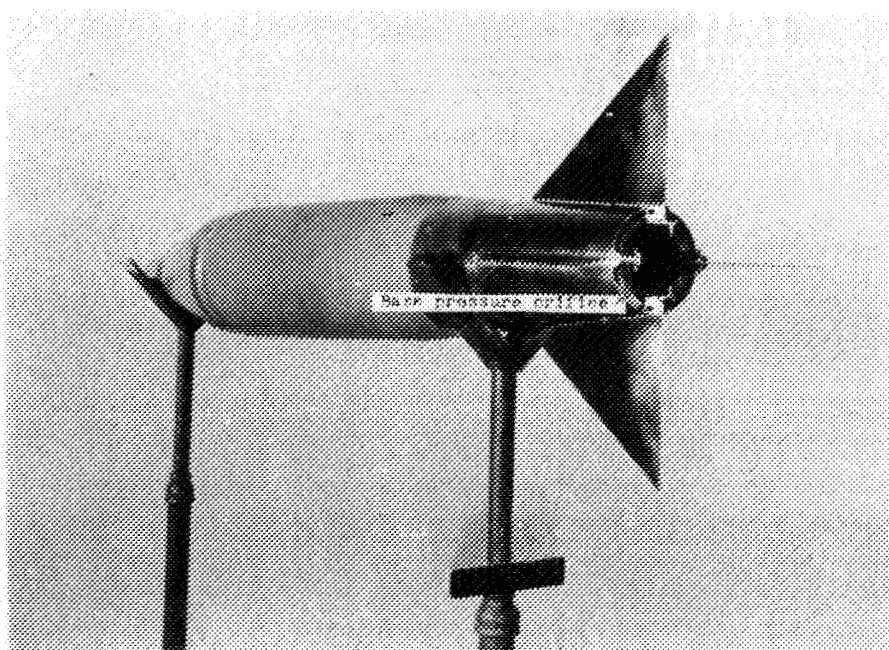
(b) Model B.   L-83835.1

Figure 3.- Rear views of drag models.
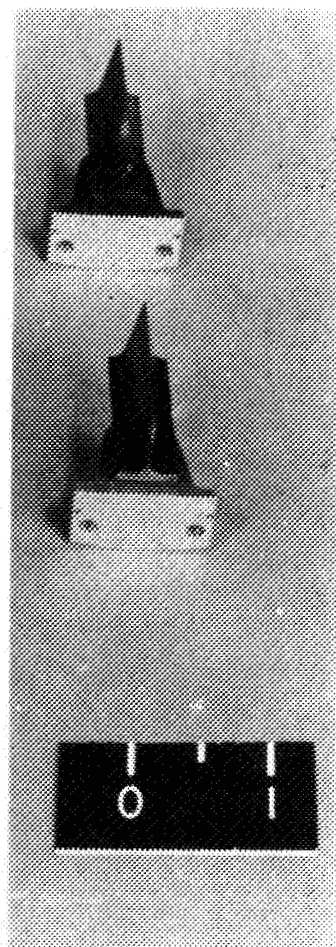
After static test

Before static test
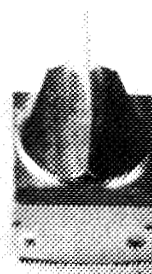
L-87991

(a) Type of jet vane used for drag   (b) Type of jet vane used for drag
     models A(1) and A(2).   models A(3) and B.

Figure 4.- Effect of rocket jet on jet vanes.
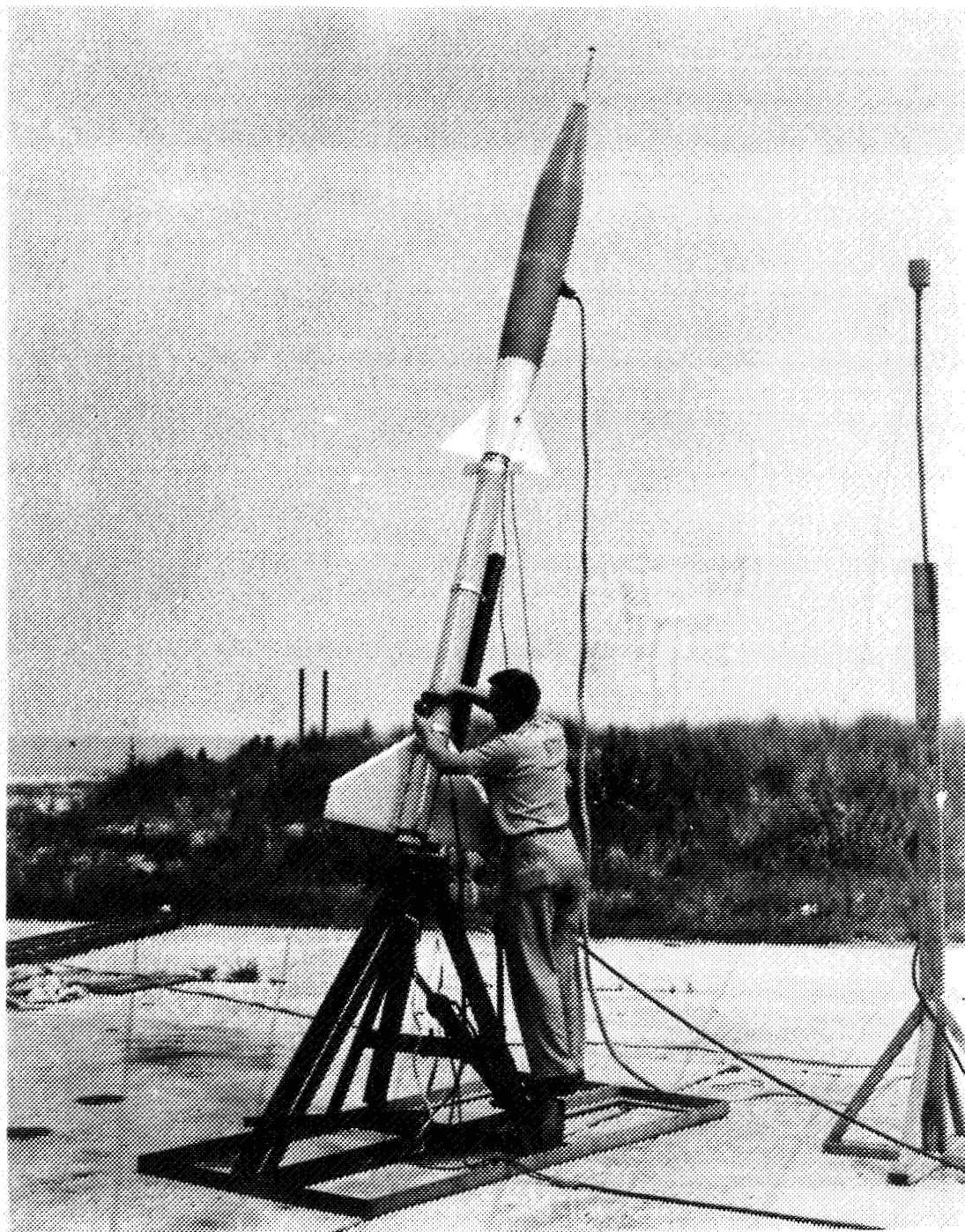
L-81060.1

Figure 5.- Typical model-booster arrangement on launching stand. Stability
model B with 65-inch-long HVAR booster.
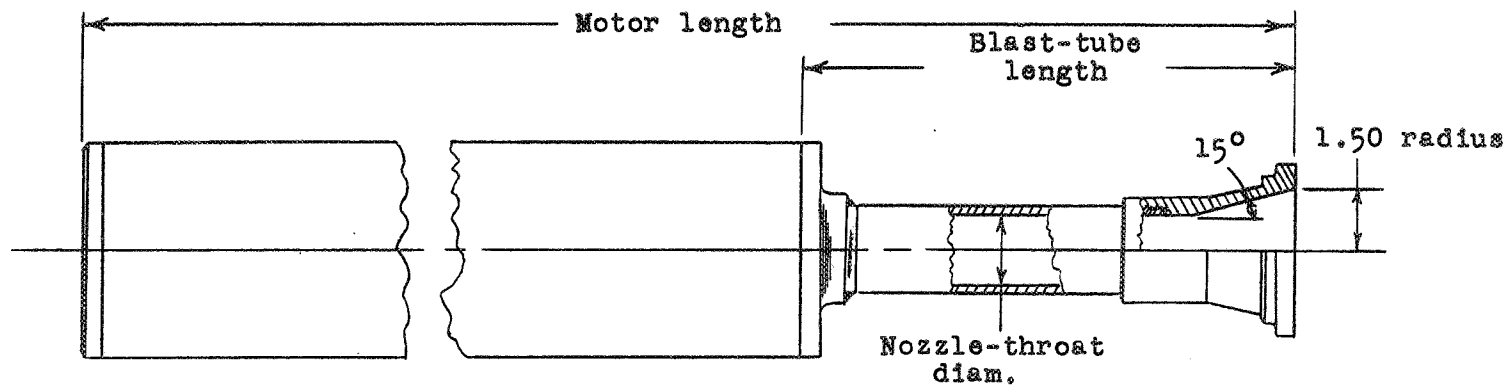
Model	Motor length	Blast-tube length	Nozzle-throat diam.	Nozzle area ratio,A_e/A_t	M_j	Burning time, sec
A(1)	38.957	11.332	1.510	3.95	2.685	4.4
A(2)	37.832	9.949	1.680	3.19	2.507	3.3
A(3)	38.882	7.740	1.635	2.38	2.552	3.1
B	51.875	10.750	1.690	3.15	2.498	2.9

Figure 6.- Various 5-inch Cordite sustainer modifications utilized in
testing the drag models. Dimensions are in inches.
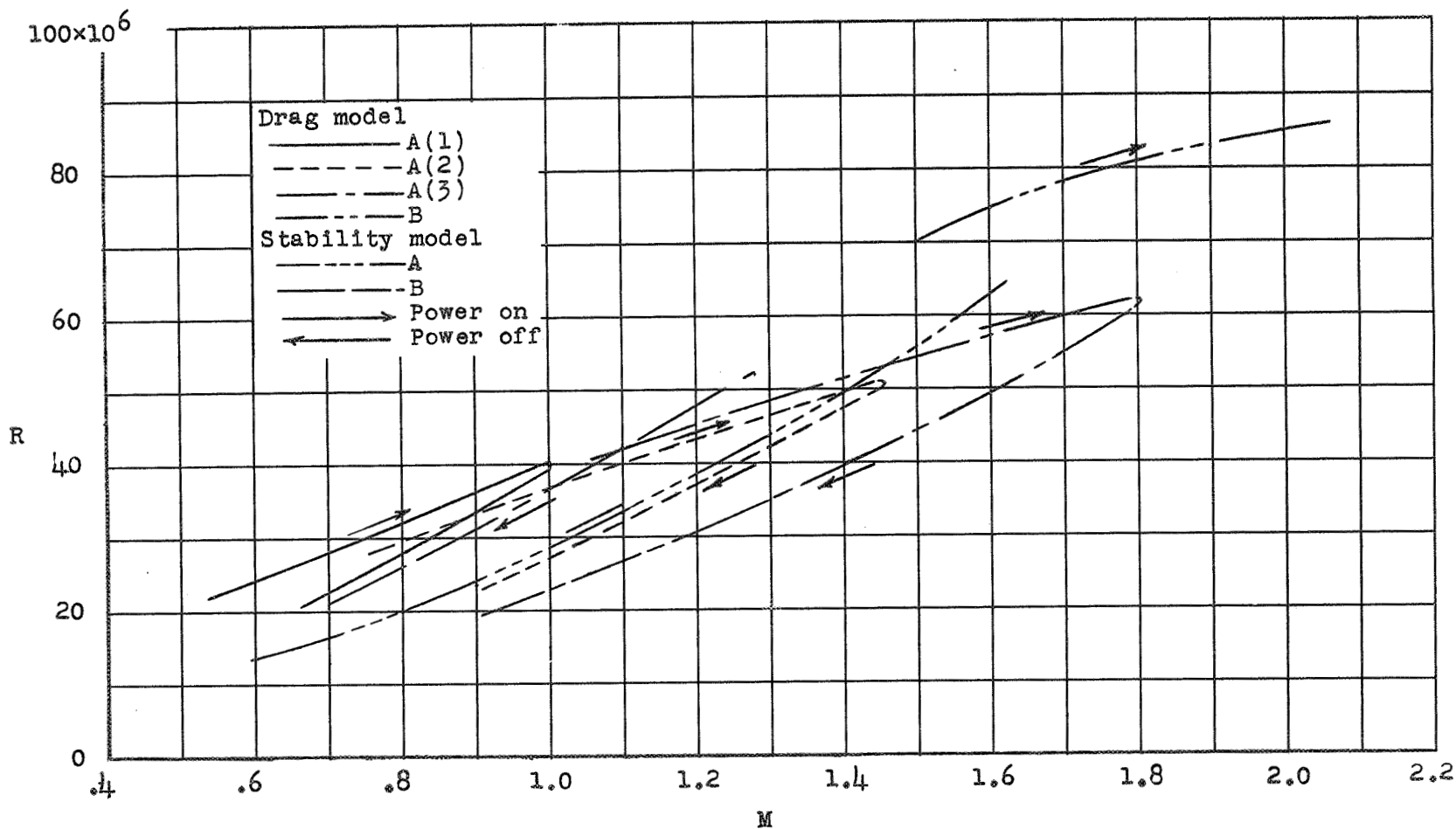
Figure 7.- Variation of Reynolds number with Mach number for the test models. Reynolds number is based on total body length.
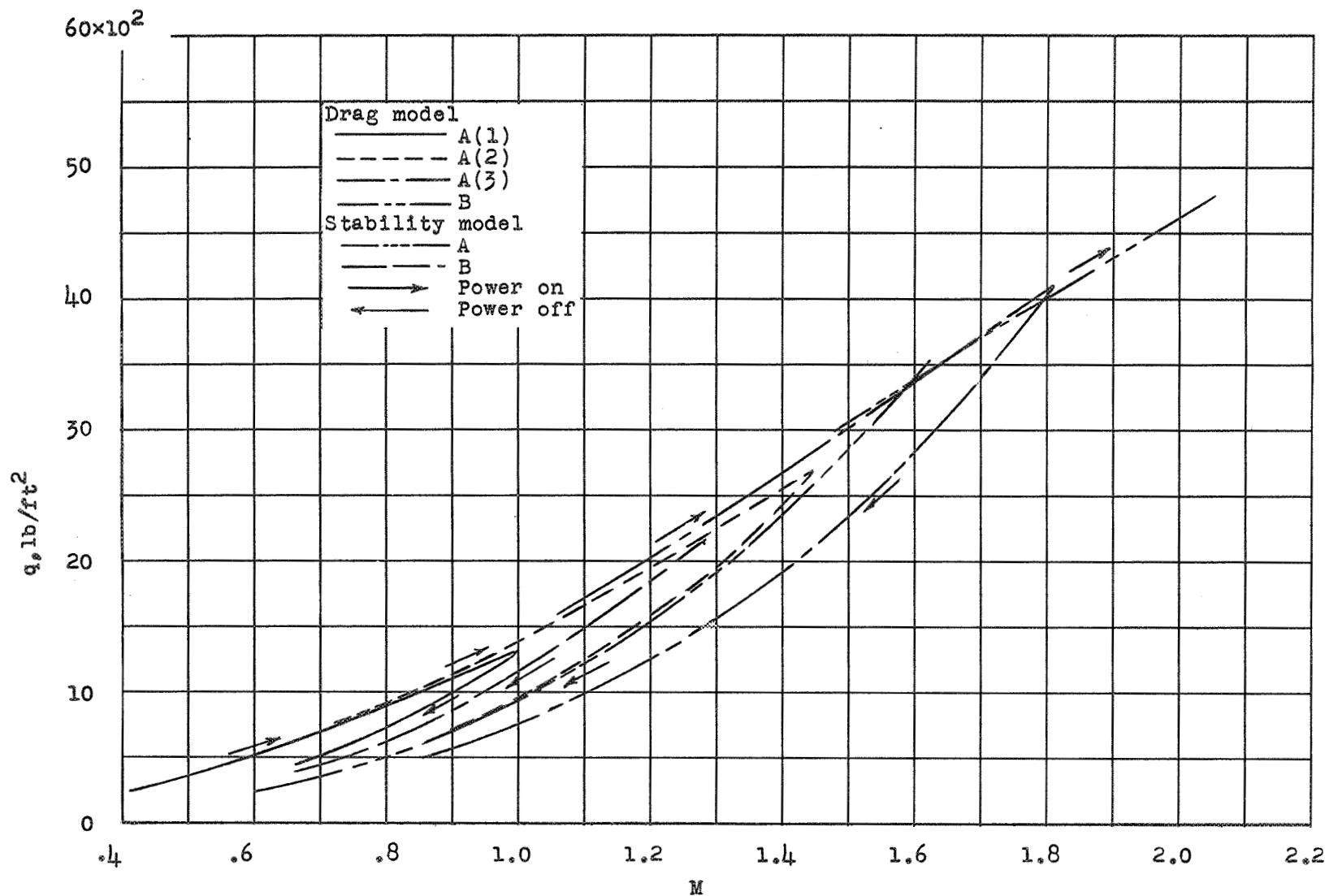
Figure 8.- Variation of dynamic pressure with Mach number for the test models.
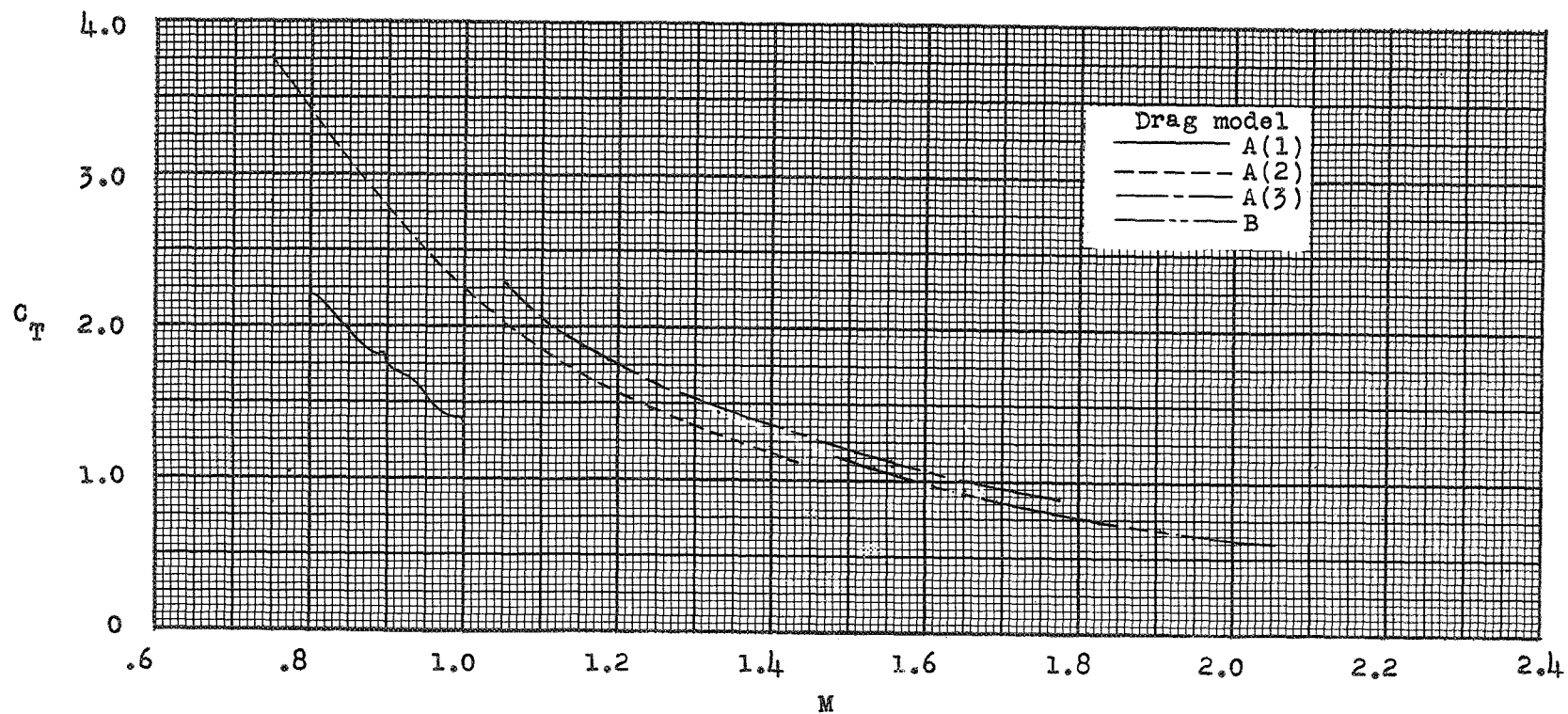
Figure 9.- Variation of thrust coefficient with Mach number for the drag
models.   Thrust coefficient is based on body frontal area.
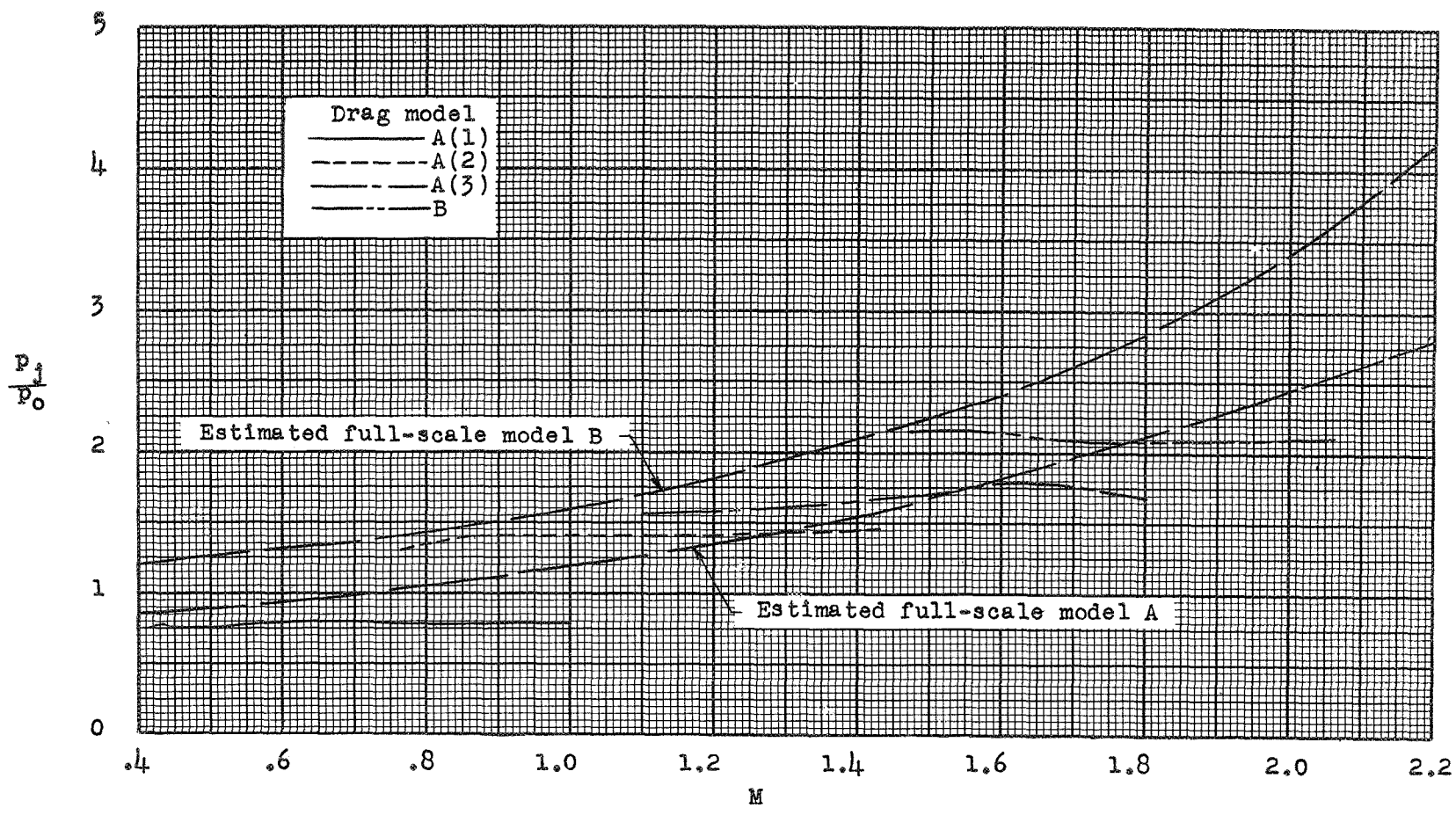
Figure 10.- Variation with Mach number of the ratio of jet-exit pressure
to free-stream pressure for the drag models.

(a) Stability model A, δ_H = 2.05°.

Figure 11.- Variation of normal-force coefficient with angle of attack.
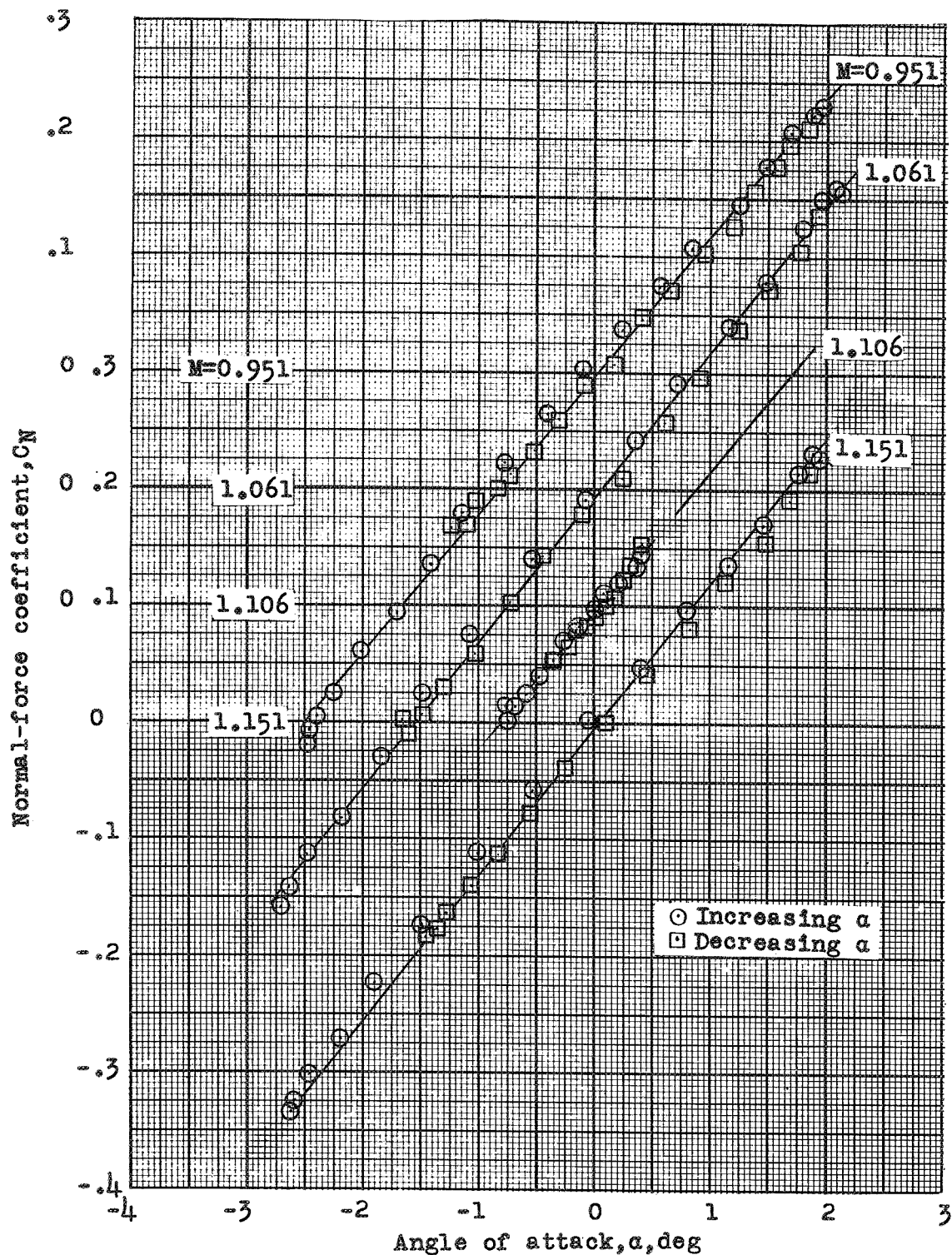
(b) Stability model B, δ = 0°.

Figure 11.- Concluded.
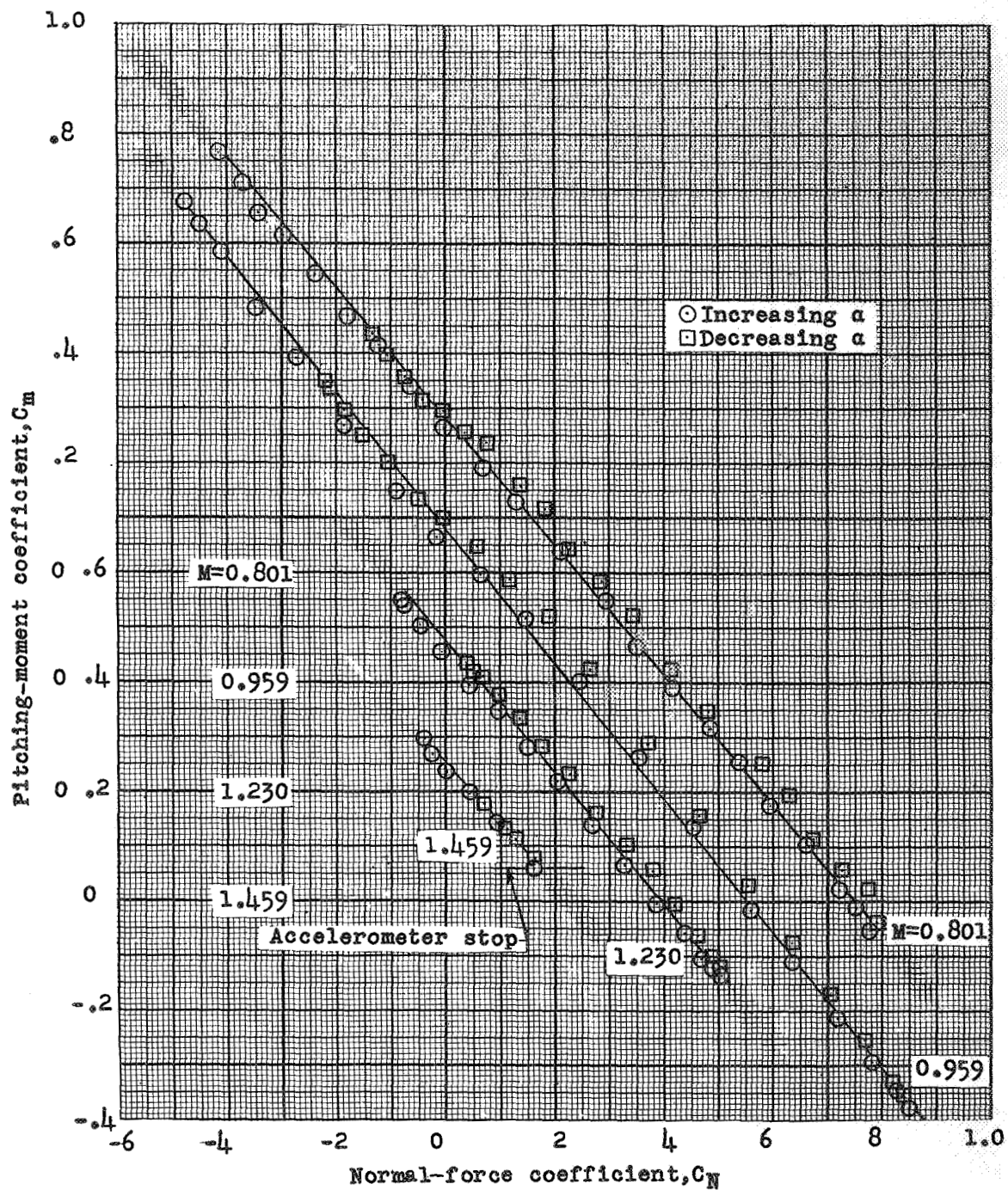
(a) Stability model A, $\delta_H = 2.05^\circ$.

Figure 12.- Variation of pitching-moment coefficient with normal-force coefficient.
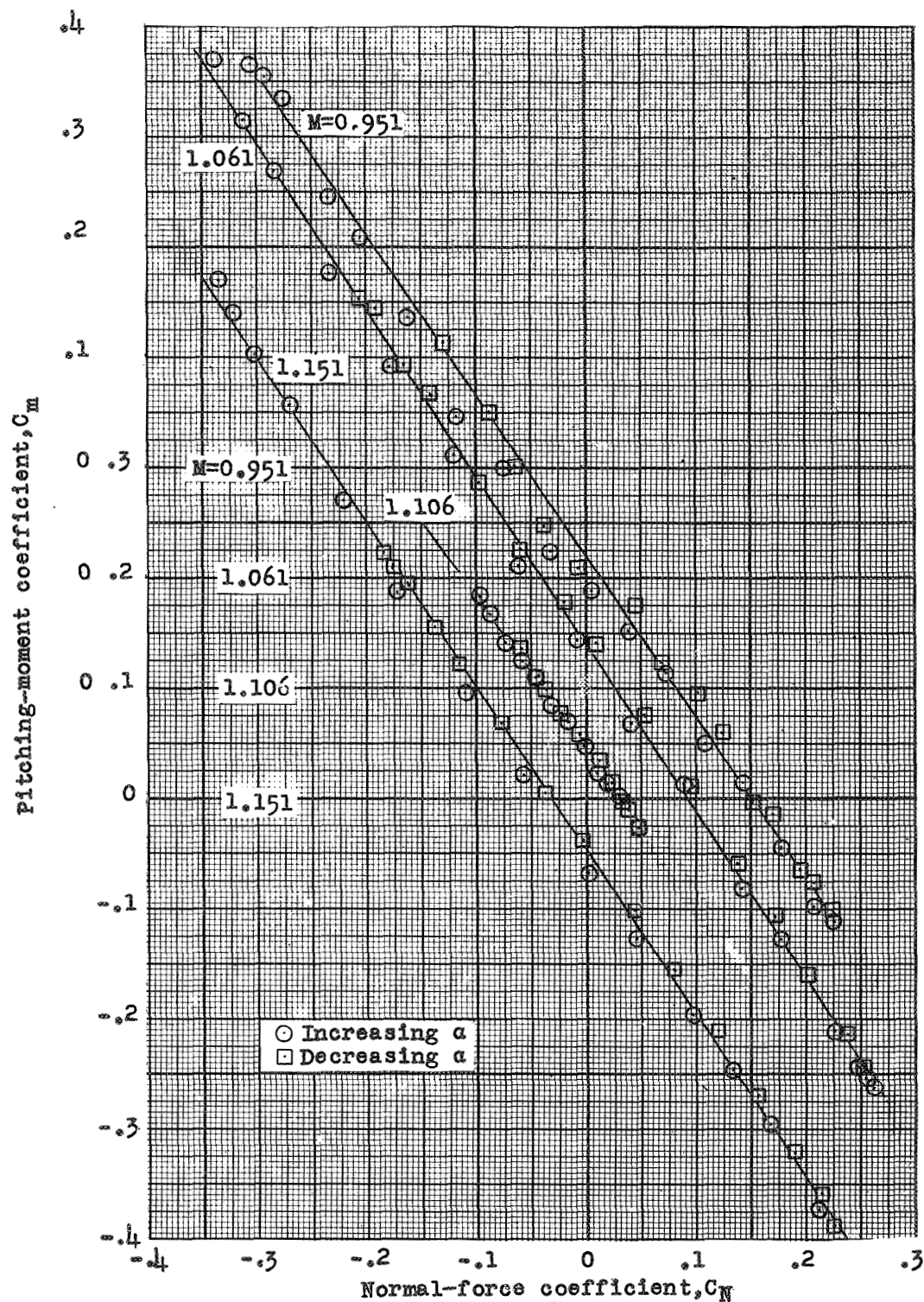
(b) Stability model B, δ = 0°.

Figure 12.- Concluded.
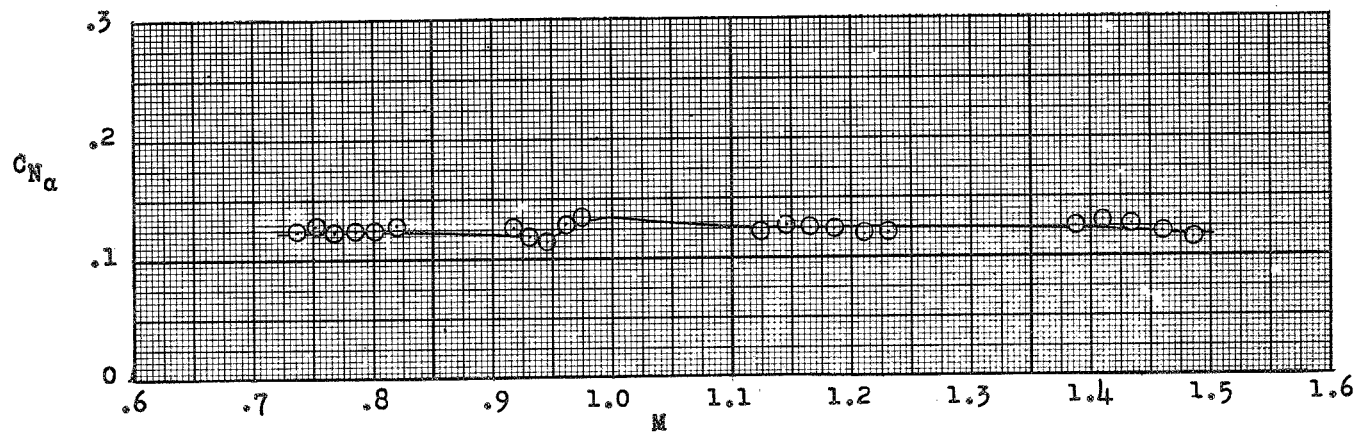
(a) Model A, $\delta_H = 2.05^\circ$.
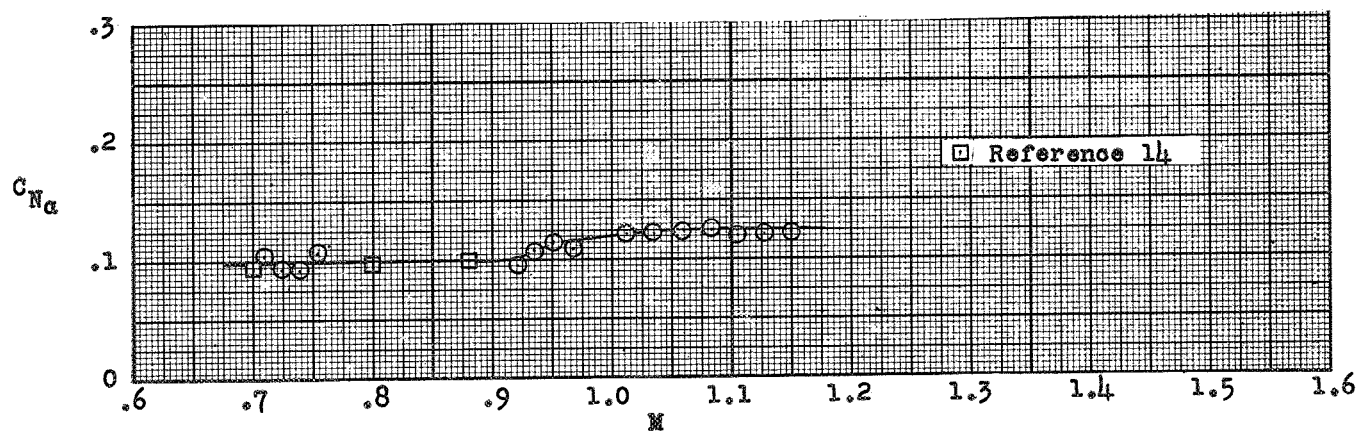
(b) Model B, $\delta = 0^\circ$.

Figure 13.- Variation of normal-force-coefficient slopes with Mach number
for stability models A and B.
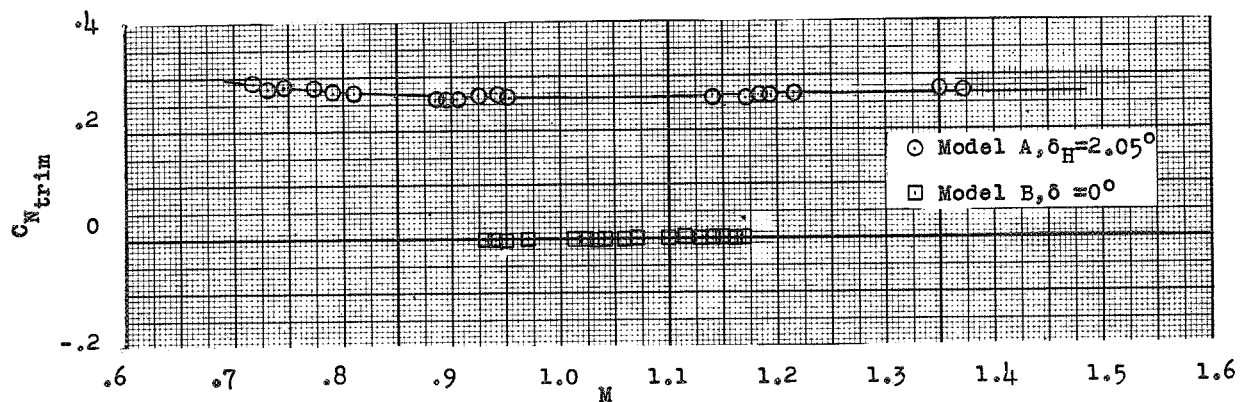
(a) Trim normal-force coefficient.
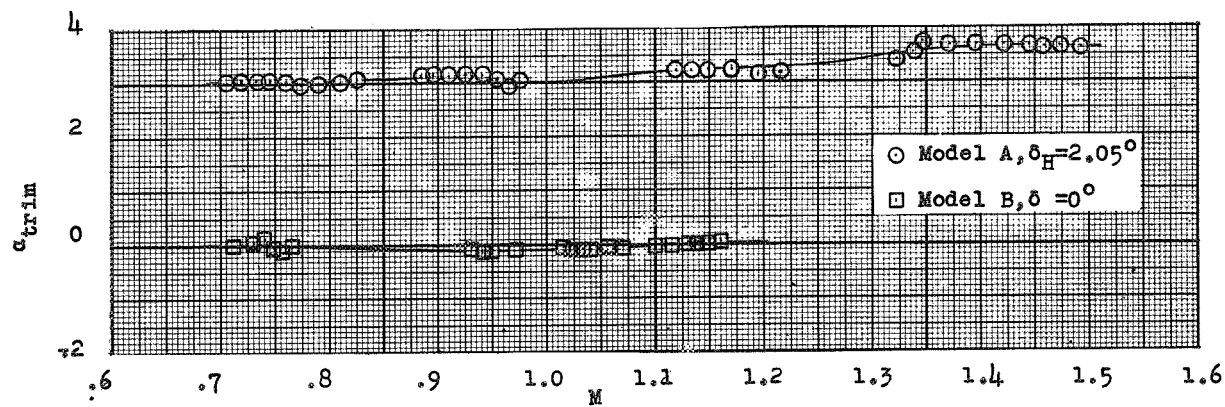
(b) Trim angle of attack.

Figure 14.- Longitudinal trim characteristics as a function of Mach number for stability models A and B.
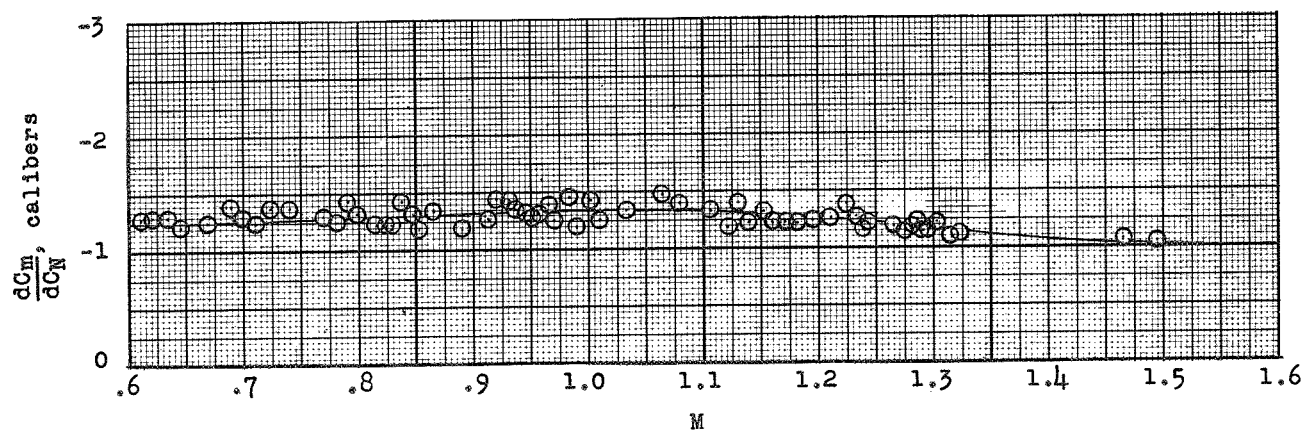
(a) Stability model A, $\delta_H = 2.05^\circ$ (c.g. = 5.377 calibers aft).
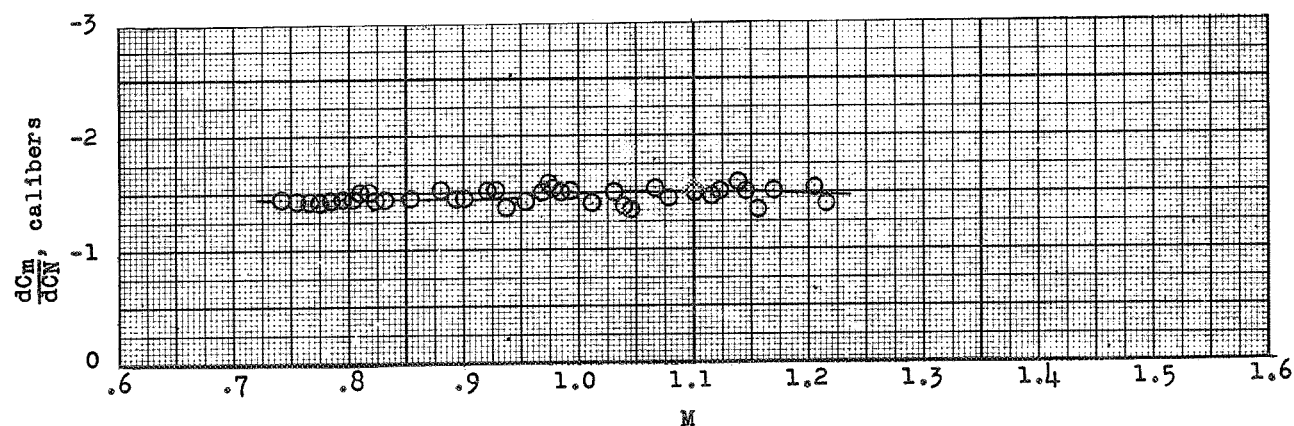
(b) Stability model B, $\delta = 0^\circ$ (c.g. = 4.869 calibers aft).

Figure 15.- Variation with Mach number of the static-longitudinal-stability parameter as obtained from two normal accelerometers.
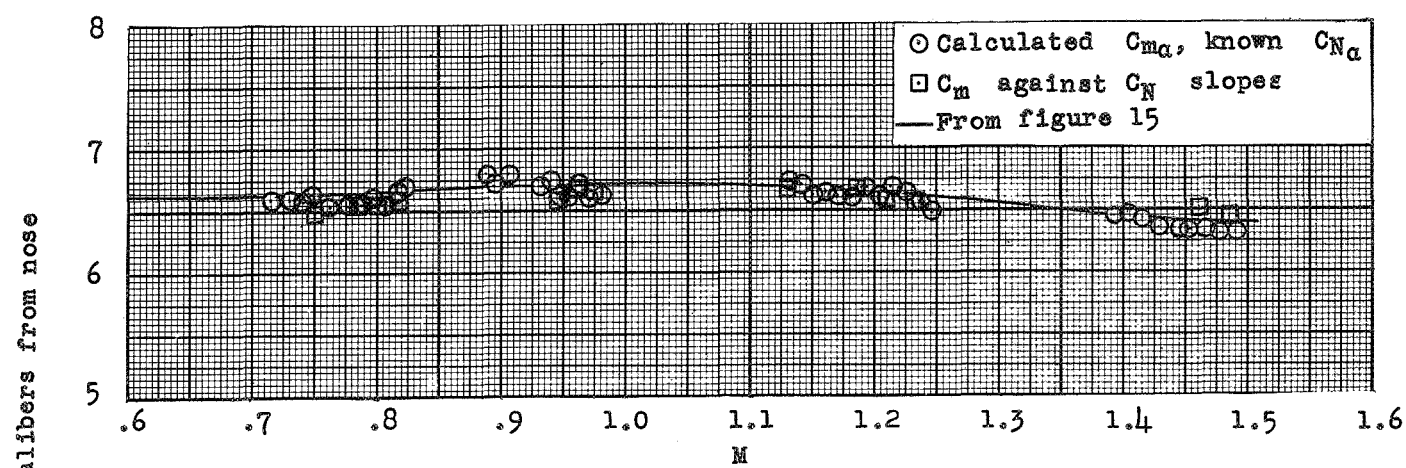
(a) Model A, $\delta_H = 2.05^\circ$.
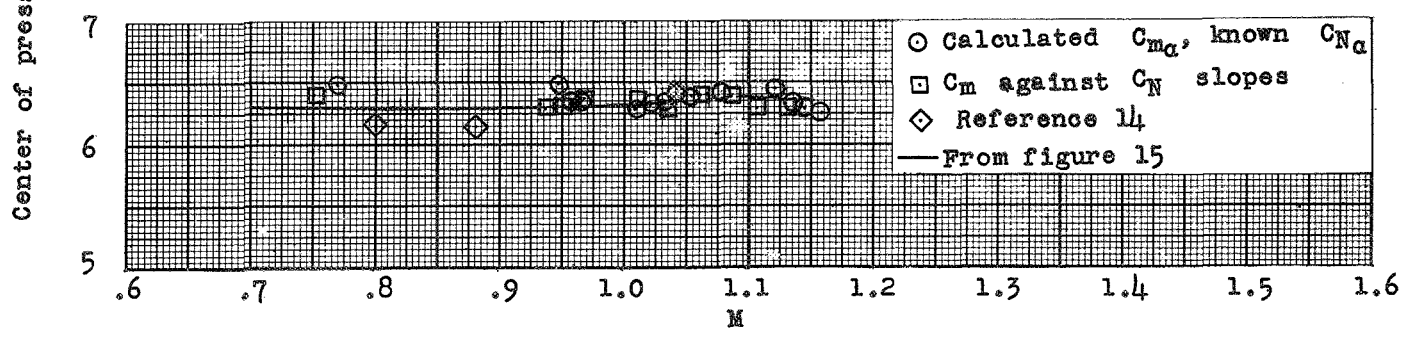
(b) Model B, $\delta = 0^\circ$.

Figure 16.- Variation of center-of-pressure location with Mach number for stability models A and B.
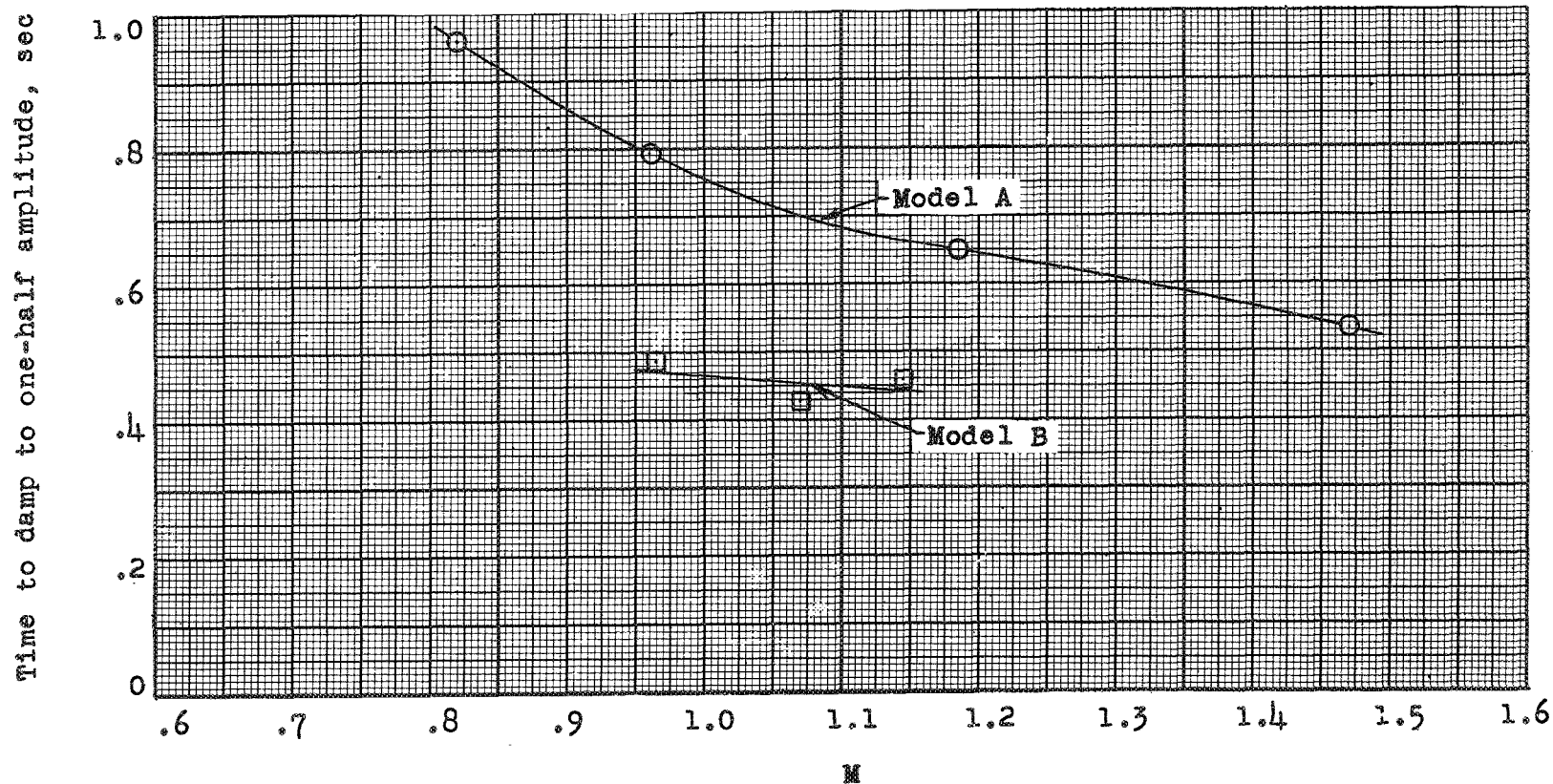
Figure 17.— Times required for the short-period oscillations to damp to one-half amplitude as a function of Mach number for stability models A and B.
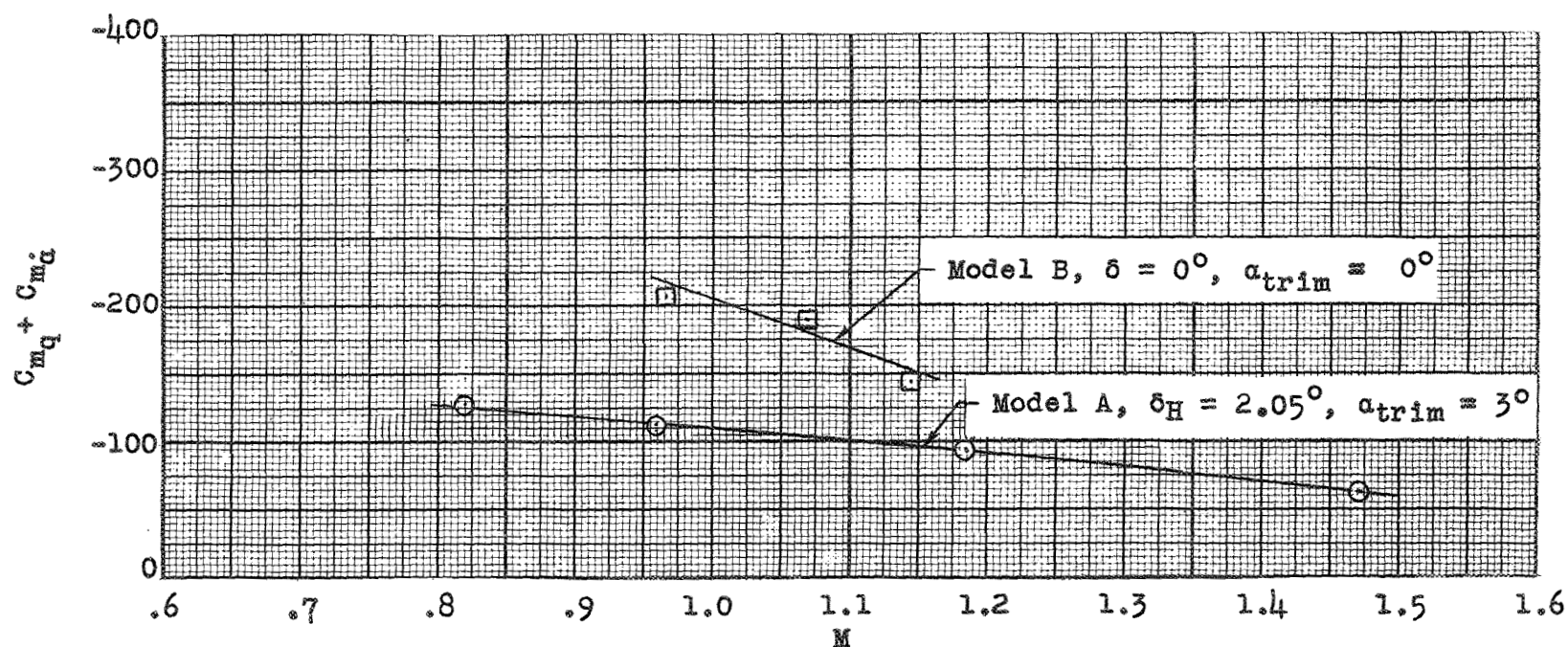
Figure 18.- Variation of damping-in-pitch derivative with Mach number for stability models A and B. Damping-in-pitch derivative determined from resultant of C_Y and C_N.
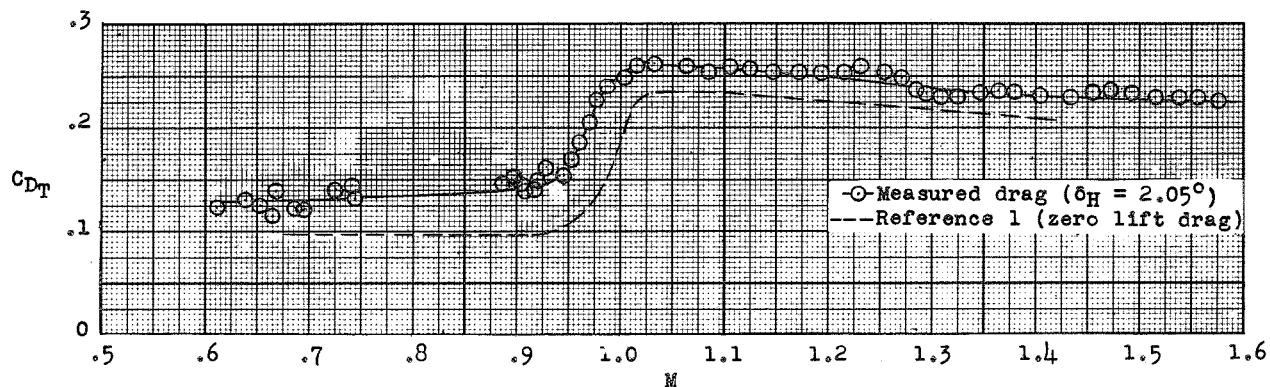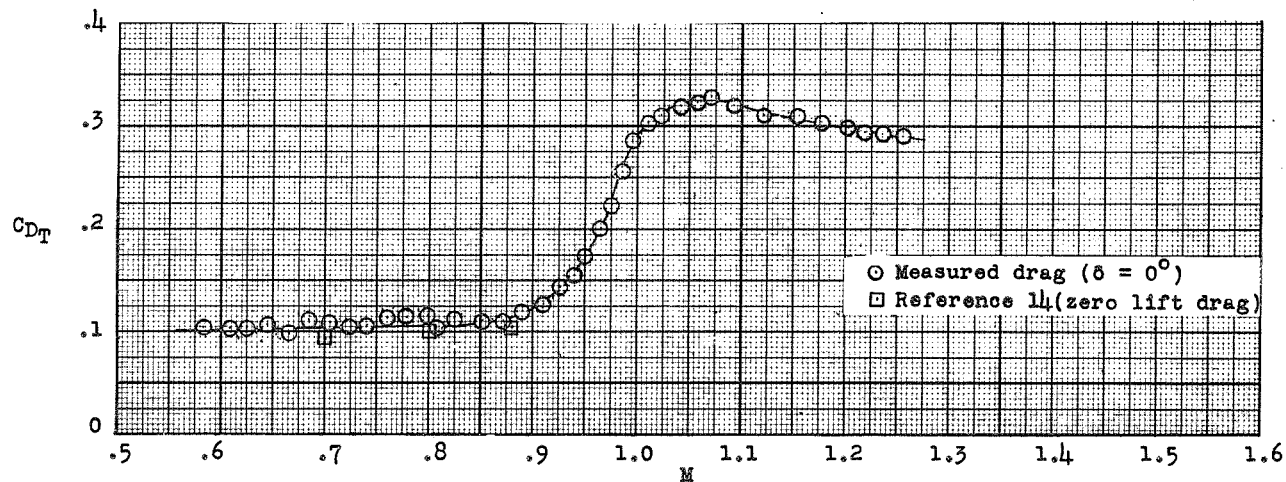
(a) Model A.

(b) Model B.

Figure 19.- Variation of total drag coefficient with Mach number for
stability models A and B.
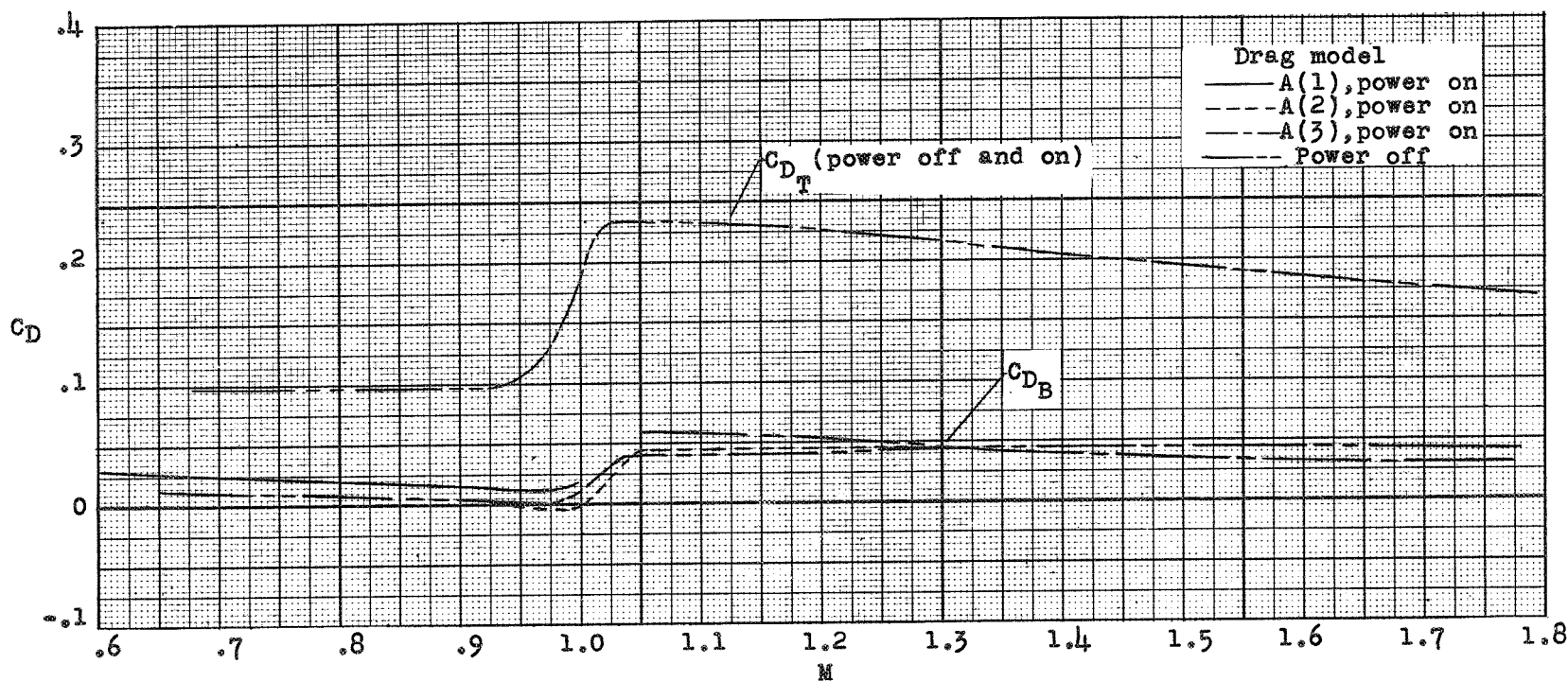
Figure 20.- Variation of total drag coefficient and base drag coefficient
(power on and power off) with Mach number for the A drag models.
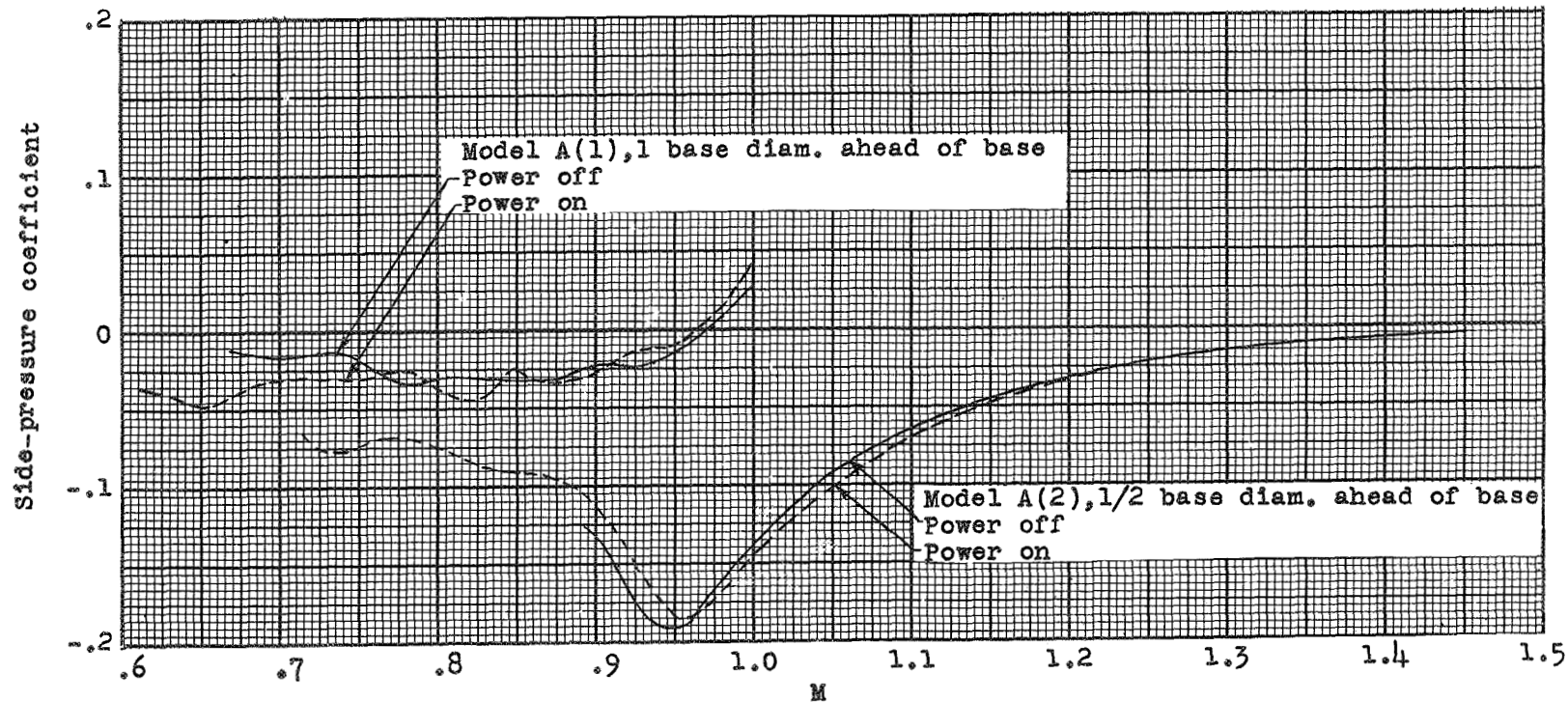
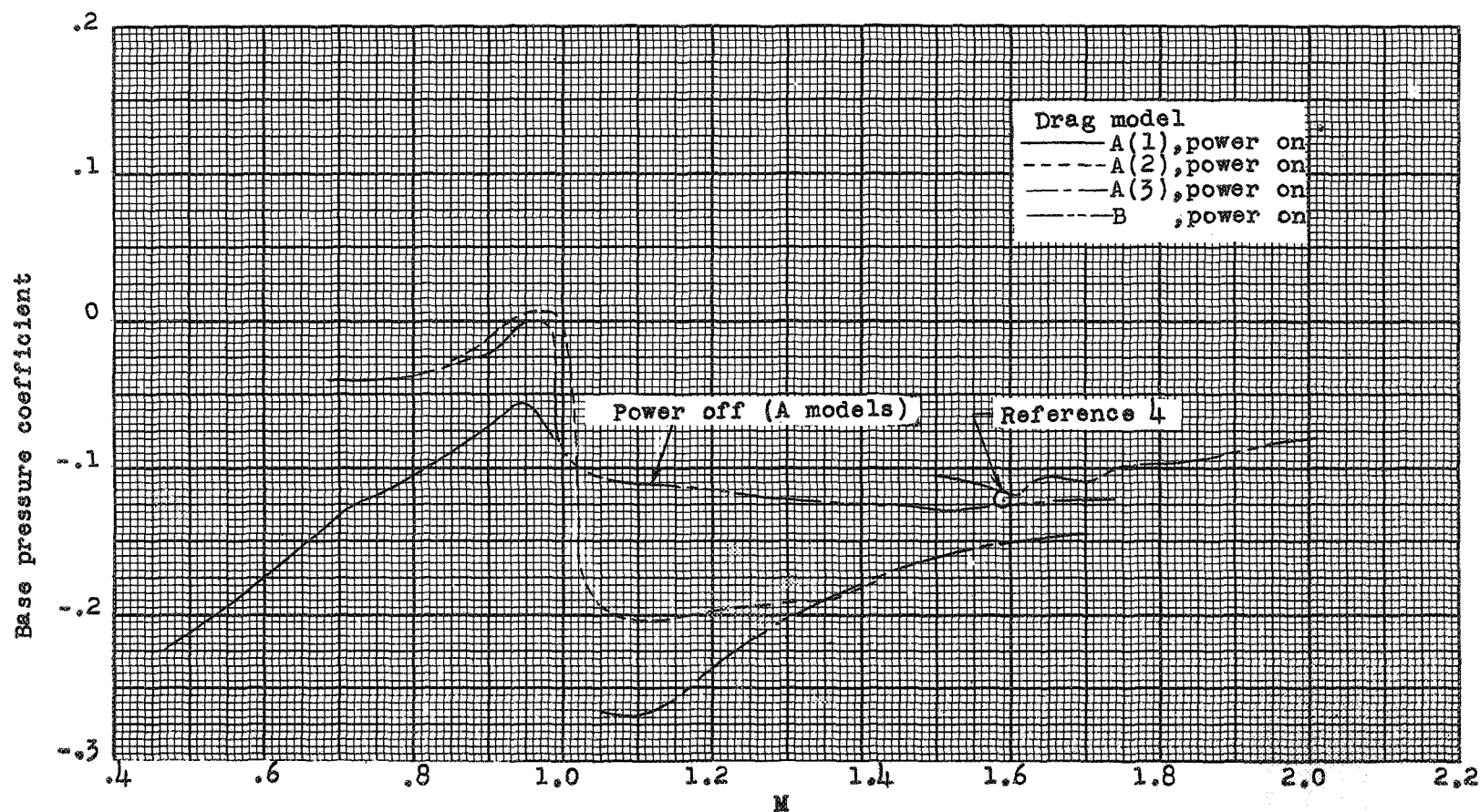Figure 21.- Variation of side-pressure coefficient with Mach number for drag models A(1) and A(2).

Figure 22.- Variation of base pressure coefficient (power on and power off) with Mach number for the drag models.